**Citation:** Papoutsakis, A., Rybdylova, O. D., Zaripov, T. S., Danaila, L., Osiptsov, A. N. & Sazhin, S. S. (2018). Modelling of the evolution of a droplet cloud in a turbulent flow. International Journal of Multiphase Flow, 104, pp. 233-257. doi: 10.1016/j.ijmultiphaseflow.2018.02.014

**Link to published version:** https://doi.org/10.1016/j.ijmultiphaseflow.2018.02.014

# Modelling of the evolution of a droplet cloud in a turbulent flow

Andreas Papoutsakis[a,*], Oyuna D. Rybdylova[a], Timur S. Zaripov[a,b], Luminita Danaila[c], Alexander N. Osiptsov[d],
Sergei S. Sazhin[a]

[a] *Sir Harry Ricardo Laboratories, Advanced Engineering Centre, School of Computing, Engineering and Mathematics, University of Brighton, Brighton, BN2 4GJ, UK.*
[b] *High Performance Distributed Computing Laboratory, Kazan Federal University, 420097, Kazan, Russia*
[c] *CORIA, UMR 6614, Université de Rouen, Avenue de l'Université, BP 12, 76801 Saint Etienne du Rouvray, France*
[d] *Institute of Mechanics, Lomonosov Moscow State University, Michurinskii 1, 119899, Moscow, Russia*

## Abstract

The effects of droplet inertia and turbulent mixing on the droplet number density distribution in a turbulent flow field are studied. A formulation of the turbulent convective diffusion equation for the droplet number density, based on the modified Fully Lagrangian Approach, is proposed. The Fully Lagrangian Approach for the dispersed phase is extended to account for the Hessian of transformation from Eulerian to Lagrangian variables. Droplets with moderate inertia are assumed to be transported and dispersed by large scale structures of a filtered field in the Large Eddy Simulation (LES) framework. Turbulent fluctuations, not visible in the filtered solution for the droplet velocity field, induce an additional diffusion mass flux and hence additional dispersion of the droplets. The Lagrangian formulation of the transport equation for the droplet number density and the modified Fully Lagrangian Approach (FLA) make it possible to resolve the flow regions with intersecting droplet trajectories in the filtered flow field. Thus, we can cope successfully with the problems of multivalued filtered droplet velocity regions and caustic formation. The spatial derivatives for the droplet number density are calculated by projecting the FLA solution on the Eulerian mesh, resulting in a hybrid Lagrangian-Eulerian approach to the problem. The main approximations for the method are supported by the calculation of droplet mixing in an unsteady one-dimensional flow field formed by large-scale oscillations with an imposed small-scale modulation. The results of the calculations for droplet mixing in decaying homogeneous and isotropic turbulence are validated by the results of Direct Numerical Simulations (DNS) for several values of the Stokes number.

*Keywords:* Fully Lagrangian Approach, turbulent diffusion, droplet mixing, second order structure, caustics

## 1. Introduction

The analysis of droplet dynamics and their spatial distribution in turbulent flows is important for various engineering applications, ranging from fuel injection in internal combustion engines to droplet dispersion in environmental flows (e.g. Sazhin (76)). Inertial droplets suspended in turbulent flow fields undulate under the influence of flow fluctuations along their trajectories. The droplet velocities are controlled by both the history of the droplet motion and the spatially correlated structures of the turbulent flow field. A variety of characteristic responses of the discrete phase to the turbulent fluctuations of the carrier phase have been identified. These responses include the macroscopic scale turbulent mixing (Fung et al. (27)), de-mixing or un-mixing of particles (Fessler et al. (22), Reeks (70)), Random Uncorrelated Motion (RUM) (Meneguz and Reeks (51)) and increasing settling velocity (Wang and Maxey (89), Maxey (49)). In large-scale engineering and environmental applications, the behaviour of sufficiently low-inertia droplets/particles, characterised by small values of the Stokes number (the ratio of the droplet velocity relaxation time to the macro time scale) in turbulent flows, has been successfully described by the convective diffusion equation with different models for the turbulent diffusion coefficient (Fuchs (25), Berlyand (3)).

---

[*] Corresponding author, email: a.papoutsakis@brighton.ac.uk

Two approaches are commonly used for the analysis of turbulent droplet/particle laden flows: Eulerian-Eulerian and Eulerian-Lagrangian (see Marchioli (46), Simonin et al. (81)). In the Eulerian-Eulerian approach several versions of the two-fluid $k - \varepsilon$ model have been used (Pakhomov and Terekhov (58)). The Eulerian-Eulerian approach gives satisfactory results for describing large-scale structures and some integral parameters of turbulent gas-particle flows in channels, jets, and boundary layers. In this approach, uniqueness of all parameters of the particulate continuum is assumed. However, the mesoscale flow regions with possible formation of local droplet accumulation zones are associated with intersecting droplet trajectories and caustics in the dispersed-phase velocity field. The appearance of local regions of intersecting droplet trajectories with singularities in the droplet number density on the edges of these regions (caustics), and the types of these singularities in non-uniform and unsteady flows with inertial droplets, were described by Osiptsov (56). Further investigations can also be found in Falkovich et al. (19) and Wilkinson et al. (90). Classes of two-particle models that allow for singularities in the phase space and intersecting trajectories (see Zaichik and Alipchenkov (93, 94), Chun et al. (14), Gustavsson and Mehlig (31), Pan and Padoan (59)), are presented in (6, 5). Also, Eulerian models for the particulate continuum inferred from the kinetic equations for particles or from the equations for the probability density functions (PDF) of particles are presented by Zaichik et al. (95) and by Shrimpton et al. (80). In engineering publications on turbulent gas-droplet flows, the carrier flow field has been described on the filtered scale, with the system of droplets described in the framework of the continuum approximation (e.g. Volkov and Emelianov (87)).

In many engineering applications (e.g. fuel spray injection and mixing, two-phase flows in combustion chambers), it is important to have information about the structure of local particle/droplet accumulation zones to estimate the rates of possible droplet collisions and the effect of droplet accumulation on heating and evaporation of droplets and combustion of fuel vapour/air mixtures (76). This information can be inferred only from Lagrangian tracking of the dispersed phase. In the standard Eulerian-Lagrangian approach for gas-particle/droplet flow modelling (e.g. Crowe et al. (16); Sazhin (76)), the carrier-phase flow parameters are calculated on a fixed Eulerian mesh and the particles/droplets are tracked along chosen Lagrangian trajectories. Direct modelling of individual droplet trajectories in the carrier phase leads to satisfactory results for the droplet velocity field (e.g. Sazhina et al. (77)). However, the correct calculation of the droplet number density field presents serious difficulties. This was instructively demonstrated by Healy and Young (35), who showed that to reach a satisfactory accuracy in the calculation of the droplet number density in a laminar flow it is necessary to have about $10^3$ Lagrangian droplet trajectories per Eulerian cell.

An approach that incorporates the solution of the droplet number conservation equation in Lagrangian form is the Fully Lagrangian Approach (FLA). In the paper by Healy and Young (35) it was demonstrated for laminar flows that the number density of non-colliding particles along a chosen particle trajectory, and the trajectory itself, can be much more efficiently calculated based on the Fully Lagrangian Approach (FLA) proposed by Osiptsov (56) (see also (Osiptsov (57))). FLA is based on the Lagrangian form of the continuity equation for the particulate phase, treated as a continuum, and the additional equations for the components of the Jacobi matrix of transformation from the Eulerian to the Lagrangian coordinates. This is essentially a method of characteristics for the solution of the continuity equation on the Lagrangian trajectories. This approach can deal with such complex cases as the regions of intersecting droplet trajectories and caustics. In (39), the efficiency of the FLA for the calculation of the droplet number density and its modelling capability in identifying the spatial structure of caustics was demonstrated.

The introduction of the FLA into the study of turbulent flows (see Picciotto et al. (65)) resulted in the identification and analysis of spatial structures of the dispersed phase distribution using the moments of concentration. The analysis by Meneguz and Reeks (51) showed that the distribution of the particle concentration in the long term is log normal. This is consistent with the analysis by Monchaux et al. (53) where, using Voronoï tessellation, the authors observed the same log normal distribution. Also, FLA studies on DNS of homogeneous and isotropic turbulence led to identification of the mechanisms involved in the segregation process (51, 70). The introduction of the FLA in the study of turbulent flows resulted in the quantification of the singularities related to trajectory intersections and the establishment of a relation between the frequency of their occurrence and the Stokes number.

The application of FLA in the Eulerian-Lagrangian context for gas-droplet flows, makes it possible to drastically reduce the number of calculated droplet trajectories, since in this case it is sufficient to have only one Lagrangian trajectory per Eulerian cell (or fold in an Eulerian cell) to ensure the required level of accuracy in the calculation of droplet concentration. This method has been successfully used for calculations concerning particle/droplet concentration fields in various flows (e.g. Tsirkunov et al. (86), Golubkina et al. (29), Govindarajan et al. (30), Wang et al. (88), Lebedeva and Osiptsov (42), Ravichandran and Govindarajan (67)).

Lebedeva et al. (43) proposed a method based on a combination of the Lagrangian viscous-vortex method for the carrier phase and the Fully Lagrangian Approach for the dispersed phase. This is the fully mesh-less approach which makes it possible to avoid a cumbersome procedure of remeshing the dispersed phase parameters from the Eulerian to Lagrangian grids, which is typical for standard Eulerian-Lagrangian approaches.

In some publications (e.g. Picciotto et al. (65), Meneguz and Reeks (51), Reeks (70)), the Fully Lagrangian Approach for the dispersed phase was used alongside the DNS calculations of the carrier phase flow fields in a turbulent channel flow and in forced homogeneous turbulence simulations. These authors identified the formation of multiple singularities in the particle concentration fields.

Note that the carrier-phase velocity fluctuations lead to increased dispersion of suspended particles/droplets (hereafter referred to as droplets) which can be identified as turbulent mixing (see Reeks (68)). Analogies between the mixing of droplets in turbulent flows and Brownian diffusion have been drawn by Xia et al. (92) and Fung et al. (27). This allows one to assume that the interaction between discrete phase and small scale turbulent fluctuations can be regarded as a Fickian diffusion process. Also, it has been observed that coherent turbulent structures of the carrier phase induce segregation of droplets at least at the level of the integral length scale of the flow field (Fessler et al. (22)), and the formation of patterns as described by Wood et al. (91), and by Soldati and Marchioli (82).

Droplet dispersion in turbulent droplet laden flows has been found to be far more sophisticated than the scalar mixing of a contaminant in a turbulent flow field (see Reeks (68), Fessler et al. (22)). It was shown that the turbulence of the carrier phase is responsible not only for droplet turbulent mixing (Fickian diffusion) (see Phythian (64)), but also for the un-mixing of droplets to form coherent structures controlled by the integral length scale of the turbulent flow field (see Fessler et al. (22), Ijzermans et al. (38)) and their accumulation in caustic formations. Thus, mixing and un-mixing processes in this case can co-exist (Xia et al. (92)).

In addition to mixing, dispersed flows exhibit a wide range of responses to the fluctuation of the carrier phase flow field. With increasing droplet inertia (Stokes number), the effects of memory on the droplet motion become more pronounced. Direct numerical simulation of the behaviour of inertial droplets in forced isotropic turbulence shows that, as a rule, the distribution of inertial droplets in a turbulent velocity field is markedly non-uniform. Maxey (49) identified the segregation of droplets by a 'preferential concentration' clustering mechanism (34), in the regions of high strain rate for small Stokes numbers. This clustering is correlated with the underlying instantaneous carrier flow velocity field. Squires and Eaton (84) observed the formation of narrow local droplet accumulation regions in the zones of low vorticity and high strain rate. In a series of publications by Vassilicos *et al.* (e.g. Chen et al. (13)), the particle accumulation zones are associated with the zero-acceleration points.

High inertia droplets sample the carrier phase velocity field as a white noise (Gustavsson and Mehlig (32)), in an ergodic fashion, forming clusters due to the 'multiplicative amplification' mechanism (90, 31, 32). Recently, this multiplicative process of amplification and dilatation was identified by Meneguz and Reeks (51) as the deformation of the Lagrangian volume of the dispersed phase (Osiptsov (56)) transported along a particle trajectory. This volume may vanish at isolated singular points, giving rise to instantaneous singularities in the particle concentration field.

In the same work (51), in addition to mixing and un-mixing (clustering), a third type of characteristic response of the dispersed phase in turbulent flows, applicable to all Stokes numbers, has been suggested. This is known as Random Uncorrelated Motion (RUM). The occurrence of RUM was linked with the occurrence of singularities due to trajectory intersections related to the trajectory history. Particle motion, as the overlapping of a mesoscopic smoothly varying component and RUM, was identified in (23, 48, 97). RUM results in a multivalued velocity field of the dispersed phase due to the folding of the dispersed continuum, playing a significant role in collision processes.

The modelling challenge introduced by the presence of turbulent fluctuations in engineering flows is related to the wide range of turbulent length scales. Any flow field can be characterised by certain macroscopic scales. The turbulent cascade of the large macroscopic eddies to the smallest scales, controlled by viscosity, leads to a flow structure which is too detailed to be accurately represented. For many practical applications, the DNS of the carrier flow field is not feasible due to the complexity of the flow geometry and high Reynolds numbers. For real life flows it becomes computationally prohibitive to obtain a solution at the required resolution. Hence, filtering or averaging operators are imposed on the governing equations. The aim is to reduce the complexity of the problem by avoiding the full resolution of the whole range of turbulent scales.

Thus the problem of how to combine the calculations of the "averaged" or "filtered" turbulent flow field (obtained using Reynolds Averaged Navier-Stokes (RANS) or Large Eddy Simulation (LES) approaches) with calculations of the droplet concentration field arises. The latter needs to take into account possible intersections of "averaged" droplet trajectories and the formation of local zones of multivalued droplet parameters and caustics.

In the present study, we suggest a new approach combining LES calculations of the carrier phase flow field and the Fully Lagrangian Approach (FLA) for the dispersed phase. This is essentially a generalisation of the FLA for the analysis of droplets in filtered turbulent flows. Our approach is based on the following assumptions:

(i) in the averaged (filtered) flow of the carrier phase, droplets can be treated as a pressureless continuum;

(ii) in the droplet continuity equation written in the Lagrangian form, subgrid random fluctuations of the carrier phase velocity result in an additional mass flux, which can be described by a Fickian law with a scalar droplet turbulent diffusion coefficient;

(iii) in calculating the droplet number density along a chosen trajectory, spatial derivatives of the number density are found by projecting the FLA solution on the Eulerian mesh; this results in a hybrid Lagrangian-Eulerian approach to the problem of calculation of the droplet concentration.

Basic principles of the FLA are summarised in Section 2. The generalisation of this approach to the analysis of the evolution of a droplet cloud in a turbulent flow is presented in Section 3. The validity of some of the assumptions, on which the model described is based, is also illustrated in Section 3, using the analysis of a simple one-dimensional flow. In Section 4 the second order extension of the FLA to describe the spatial structure of the number density field is presented and demonstrated. In Section 5, numerical experiments to determine the spatial structure of a turbulent flow field in a box with homogeneous decaying turbulence are described. In the same Section the model predictions are compared with the DNS predictions. In Section 6, the motivation behind the modelling choices made for the derivation of the modified FLA is discussed. The main results of the paper are summarised in Section 7.

## 2. The Fully Lagrangian Approach

In this section we present the framework of the Fully Lagrangian Approach (FLA) used for the modelling of a particulate medium dispersed in a fully resolved (laminar) carrier phase flow field. We set out the governing equations for the conservation of mass and momentum used in the FLA.

The droplets are assumed to be identical spheres of mass $m_d$ and radius $\sigma$. Assuming the point particle approximation, inter-particle collisions can be ignored. Thus, ignoring the Brownian motion of the droplets, the velocity of the dispersed phase at each point in the dispersed-phase continuum is singularly defined. This implies that the probability density function for the droplet distribution over velocities is the Dirac delta-function, and the velocity of a sampling droplet coincides with the velocity of the dispersed-phase continuum $\mathbf{V_d}$. The dispersed phase continuum is defined in a space with possible folds; thus, $\mathbf{V}_d$ can be multivalued. Hence, the trajectory of a droplet, coinciding with the trajectory of an elementary volume of the droplet continuum, is described by the following kinematic equation:

$$\frac{d\mathbf{x}^d}{dt} = \mathbf{V_d}\ . \tag{1}$$

If $\mathbf{f}$ is the force exerted on the droplet by the fluid, the velocity of the droplet continuum can be found from the momentum equation for a droplet:

$$m_d \frac{d\mathbf{V}_d}{dt} = \mathbf{f}. \tag{2}$$

Equation (2) follows from the momentum equation for a pressureless continuum, as described in (45).

Note that the very dilute particulate continuum, introduced in FLA, is in some sense ‘artificial’. This particulate continuum can penetrate itself since the droplet trajectories can intersect, forming ‘creases’ and ‘folds’. This means that the continual variable $\mathbf{V}^d(\mathbf{x}, t)$ can be multivalued, at least in some regions where droplet trajectories intersect. This makes it difficult to describe this dispersed continuum using the Eulerian approach since the momentum and continuity equations in the Eulerian variables assume that all parameters are single-valued. Alternatively, one could use the Lagrangian approach to describe the particulate medium. Equations (1) and (2) can be regarded as Lagrangian equations if the variables $(\mathbf{x}^d)$ and $\mathbf{V}^d$ are considered as the functions of Lagrangian coordinates $\mathbf{x_0^d}$ and time $t$. In what follows the continuity equation for the particulate continuum will be formulated in the Lagrangian form.

Introducing the droplet number density $n_d$ as the mean number of droplets per unit volume, we can formulate the continuity equation of the droplet medium in the integral form:

$$\frac{d}{dt}\int_{V_L(t)} n_d d\mathbf{x}^d = 0, \tag{3}$$

where, $V_L(t)$ is an arbitrary Lagrangian volume of the droplet continuum, each point of which travels at the droplet velocity $\mathbf{V}_d(\mathbf{x}^d, t)$, where $\mathbf{x}^d$ is the radius vector of the point in a Cartesian coordinate system.

Introducing Lagrangian variables $\mathbf{x}_0^d$ and $t$ ($\mathbf{x}_0^d = (x_0^d, y_0^d, z_0^d)$ are the coordinates of the radius vector of the point at the initial instant of time $t = 0$), we can rewrite this equation as:

$$\frac{d}{dt}\int_{V_0} n_d(\mathbf{x_0}, t)\det\left(J_{ij}(\mathbf{x}_0, t)\right) d\mathbf{x}_0 = 0\ , \tag{4}$$

where, $\det(J(\mathbf{x}_0, t))$ is the determinant of the Jacobi matrix for the transformation from the Eulerian to the Lagrangian coordinates, defined as:

$$J_{ij} = \frac{\partial x_i^d}{\partial x_{0,j}^d}\ , \tag{5}$$

$x_i^d$ is the $i$th component of the radius vector of the point in the droplet cloud at time instant $t$, and $x_{0,j}^d$ is the $j$th coordinate of this point at the initial time instant $t = 0$. The introduction of the Jacobian of the transformation from the Lagrangian to the Eulerian coordinates implies that the transformation $\mathbf{x}(\mathbf{x}_0, t)$ is continuous and differentiable.

In (4), the integration is performed over the initial volume $V_0 = V_L(t = 0)$. Since $V_0$ does not depend on time, the order of time differentiation and spatial integration can change. Since this equation is valid for an arbitrary volume $V_0$, the continuity equation for the droplets can be written in the differential Lagrangian form:

$$\frac{d}{dt} n_d(\mathbf{x_0}, t)\det\left(J_{ij}(\mathbf{x}_0, t)\right) = 0. \tag{6}$$

During the droplet cloud motion, the trajectories of the droplets may intersect and form 'folds'. In these folds, two or more values of droplet velocity and number density may correspond to the same Eulerian point $\mathbf{x}_0^d$ (Osiptsov (57)). In the Lagrangian coordinates, however, these parameters remain single-valued, since they correspond to different values of Lagrangian coordinates $\mathbf{x}_0^d$. At the edges of the folds (caustics), the Jacobian $\det(J_{ij})$ changes sign, which corresponds to the change in the orientation of an elementary Lagrangian volume. Remembering that this change of orientation should not affect the values of droplet number density, we replace the value of $\det(J_{ij})$ in (6) with its absolute value $||\mathbf{J}||$, leading to the following explicit expression for the number density (Osiptsov (57)):

$$n_d(\mathbf{x_0^d}, t)||\mathbf{J}(\mathbf{x}_0^d, t)|| = n_d(\mathbf{x}_0, 0). \tag{7}$$

This equation can be used for the analysis of droplet flows, including those with intersecting trajectories. It is more general than the standard continuity equation, written in Eulerian form, which assumes uniqueness of the droplet velocity and number density:

$$\frac{\partial n_d}{\partial t} + \mathrm{div}(n_d\mathbf{V_d}) = 0\ . \tag{8}$$

We restrict our analysis to the case when only Stokes drag is exerted on the droplets $\mathbf{f} = 6\pi\sigma\mu(\mathbf{U} - \mathbf{V}_d)$. In this case, the kinematic and momentum equations for the droplets in Lagrangian variables take the form:

$$\frac{dx_i^d(\mathbf{x}_0, t)}{dt} = V_{d,i}(\mathbf{x}_0, t), \quad \frac{dV_{d,i}(\mathbf{x}_0, t)}{dt} = \frac{1}{\tau_d}(U_i - V_{d,i}), \tag{9}$$

where

$$\tau_d = \frac{m_d}{6\pi\sigma\mu} = \frac{2\sigma^2\rho_d}{9\mu},$$

$\rho_d$ is the density of the droplet material, and $\mu$ is the dynamic viscosity of the carrier phase. The droplet number density $n_d(\mathbf{x}_0, t)$ can be found from the Lagrangian continuity equation (7).

We can derive additional equations for the components $J_{ij}$ by differentiating Equations (9) with respect to the Lagrangian coordinates and changing the order of differentiation with respect to space coordinates and time (Osiptsov (57)). As a result, we obtain the following equations:

$$\frac{dJ_{ij}(\mathbf{x}_0, t)}{dt} = \omega_{ij} \ , \tag{10}$$

where $\omega_{ij}$ are the auxiliary variables inferred from the following equations:

$$\frac{d\omega_{ij}(\mathbf{x}_0, t)}{dt} = \frac{1}{\tau_d}\left(J_{kj}\frac{\partial U_i}{\partial x_k} - \omega_{ij}\right) \ . \tag{11}$$

For a fixed droplet trajectory (fixed value of $\mathbf{x}_0$) Equations (7), (9), (10) and (11) constitute a closed system of ordinary differential equations. The solution to this system, with corresponding initial conditions $\mathbf{x}_0^d, \mathbf{V_{d0}}, J_{ij0}$, and $\omega_{ij0}$ at the origin of the droplet trajectory, gives the coordinates of this trajectory, the droplet velocity and the values of the Jacobi matrix components. In this case, Equation (7) allows us to calculate the values of the droplet number density along a chosen droplet trajectory.

## 3. Droplet cloud in a filtered turbulent flow

In this section we present an adaptation of the FLA to the modelling of a droplet cloud in the LES context. We derive the FLA equations for the conservation of mass and momentum for the dispersed phase transported by a filtered carrier phase flow field. The effect of the unresolved turbulent fluctuations of the filtered carrier phase flow field will appear in the form of unclosed terms in the FLA governing equations. We suggest a closure of the turbulent flux which appears in the mass conservation equation based on standard turbulent diffusion models. Finally, we assess the effect of unresolved fluctuations on the conservation of momentum for the case of a simple one-dimensional filtered flow field.

### *3.1. The FLA equations for a filtered turbulent carrier phase flow field.*

In the LES context the turbulent velocity field $\mathbf{U}$ is decomposed into a spatially filtered velocity $\overline{\mathbf{U}}$ and the subgrid fluctuation $\mathbf{u}'$:

$$\mathbf{U} = \overline{\mathbf{U}} + \mathbf{u}' \ , \tag{12}$$

where $\bar{\cdot}$ is a spatial filtering operator defined as:

$$\overline{f}(\mathbf{x}_0, t) = \int_\Omega f(\mathbf{x}, t)G(\mathbf{x} - \mathbf{x}_0)d\mathbf{x} \ , \tag{13}$$

$\Omega$ is the computational domain, $G(\mathbf{r})$ is the filter kernel which is characterised by a spatial cutoff length scale $\Delta$. For a 'box filter' $G$ is constant, $G(\mathbf{r}) = 1/\Delta^3$, and the filtering volume coincides with volume $\Omega_i$ of the LES discretisation. In this case $\Delta = \Omega_i^{1/3}$. This filter will be assumed in our analysis.

Droplets dispersing in a turbulent flow field are expected to deviate from the trajectories inferred from a certain averaged solution, due to turbulent fluctuations, resulting in a turbulent mixing of droplets as shown in Figure 1. For droplets with large inertia we can assume that large scale eddies (resolved in the filtered flow field) are the main contributors to the momentum transport of droplets (2). The small-scale fluctuations are assumed to contribute only to the transport equation for the droplet number density as discussed in Section 5. Hence, the averaged momentum equation for a sampling droplet can be written as:

$$\frac{d\overline{\mathbf{V}}_d}{dt} = \frac{1}{\tau_d}(\overline{\mathbf{U}} \ - \ \overline{\mathbf{V}}_d), \tag{14}$$

where, $\overline{\mathbf{V}}_d$ is referred to as the 'filtered' velocity of the droplet. $\overline{\mathbf{V}}_d$ is defined implicitly as the velocity inferred from the filtered flow field; it can be multivalued.

When deriving (14) the momentum transport due to the unresolved velocity fluctuations was ignored. Thus, $\overline{V_{di}V_{dj}}$ is considered equal to $\overline{V}_{di}\overline{V}_{dj}$. Having assumed that $\overline{v'_{d,i}v'_{d,j}} \ll \overline{V}_{d,i}\overline{V}_{d,j}$ we treat the system of droplets as a pressureless continuum. In this case the mean mass velocity coincides with the velocity of a sampling droplet.

Taking into account the contribution of the transport of mass due to fluctuations of droplet velocity induced by the subgrid fluctuations of the carrier phase velocity, Equation (3) can be generalised to:

$$\frac{d}{dt}\int_{V_L(t)} n_d d\mathbf{x}_d = -\int_{S_L(t)} \mathbf{j}_T dS = -\int_{V_L(t)} \mathrm{div}(\mathbf{j}_T) d\mathrm{x}_\mathrm{d}, \tag{15}$$

where $V_L$ is the Lagrangian volume of the droplet medium moving with the filtered velocity $\overline{\mathbf{V}}_d$, $S_L$ is the surface of this volume, and $\mathbf{j}_T$ is the additional flux of the droplets due to droplet velocity fluctuations induced by the subgrid fluctuations of the carrier-phase velocity. This equation is then transferred into the differential form in Lagrangian coordinates $\mathbf{x}_0$, as was done when deriving (6), leading to the following continuity equation for droplets:

$$\frac{d}{dt} n_d(\mathbf{x}_0, t)||\mathbf{J}|| = -\mathrm{div}(\mathbf{j}_T)||\mathbf{J}||, \tag{16}$$

where $||\mathbf{J}||$ is the absolute value of the determinant of the Jacobi matrix of the transformation from the Eulerian to Lagrangian coordinates for the droplet medium motion with averaged velocity $\overline{\mathbf{V}}_d$. This approximate 'filtered' description of the droplet motion is valid when the contributions of the droplet velocity fluctuations to the mass and momentum fluxes are both small, but the ratio $|\mathbf{j}_T|/n_d|\overline{\mathbf{V}}_\mathbf{d}|$ is much greater than the ratio $\overline{v'_{d,i}v'_{d,j}}/\overline{V}^2_{d,i}$. As shown later with reference to an example of a simple one-dimensional flow, this condition can be satisfied for droplets with moderate inertia (see Section 4).

We assume that Fick's law is applicable, which allows us to present $\mathbf{j}_T$ as:

$$\mathbf{j}_T = -D_T \nabla n_s, \tag{17}$$

where $D_T$ is the turbulent diffusion coefficient. Having substituted (17) into (16) we obtain the equation for droplet number density in the form of a modified convective diffusion equation:

$$\frac{d}{dt}\left(n_d(\mathbf{x}_0, t)||\mathbf{J}||\right) = \mathrm{div}(D_T \nabla n_d)||\mathbf{J}||. \tag{18}$$

To estimate the values of the turbulent diffusion coefficient of droplets $D_T$, we need to know the intensity of the turbulent fluctuations for the droplet velocities along the filtered droplet trajectories. The average energy of these fluctuations can be estimated as $k_v = 0.5 \cdot \overline{\mathbf{v}' \cdot \mathbf{v}'}$, where $\mathbf{v}'$ are fluctuations of the droplet velocities in individual computational cells. Using the above definition of $k_v$, the characteristic velocity of droplet fluctuations is estimated as $\mathcal{V} = \sqrt{2/3k_v}$.

The turbulent flux $\mathbf{j}_T$ is assumed to be driven by Fickian diffusion due to individual droplet fluctuations. Recent research on the dispersion of particles has highlighted the analogies between particle dispersion in turbulence and Brownian motion (92). The physical mechanism of Brownian motion occurs at the molecular scale and it is different from the mechanism responsible for the oscillation of droplets in a turbulent flow field. The diffusion of droplets in a turbulent field, however, is proportional to the characteristic velocity of their fluctuations, as in Brownian motion (see Section 6). Following (92), the droplet turbulent diffusion coefficient can be presented as:

$$D_T = \mathcal{V}\mathcal{L}, \tag{19}$$

where $\mathcal{V}$ and $\mathcal{L}$ are characteristic velocity of the turbulent fluctuations and their characteristic length, respectively.

The value of $\mathcal{V}$ is calculated as the product of the characteristic velocity of the carrier phase $\mathcal{U}$ and the ratio of $\mathcal{V}$ and $\mathcal{U}$ : $\lambda = \mathcal{V}/\mathcal{U}$. The carrier phase characteristic velocity stems from the subgrid turbulent kinetic energy $k_{\mathrm{sgs}} = 0.5\overline{\mathbf{u}' \cdot \mathbf{u}'}$ of the carrier phase fluctuations as $\mathcal{U} = \sqrt{2/3k_{\mathrm{sgs}}}$. Coefficient $\lambda$ can be estimated using the intensity of droplet fluctuations as a function of the turbulent intensity of the carrier phase $\mathcal{U}$. A closure for $\mathcal{V}$ can be achieved by introducing Stokes law in the expression for the characteristic velocity $\mathcal{V}$ of droplet fluctuations:

$$\frac{d\mathcal{V}^2}{dt} = \frac{1}{3}\frac{d}{dt}\overline{v'_i v'_i} = \frac{1}{3}\overline{2v'_i\frac{dv'_i}{dt}} = \frac{2}{\tau_d}\left(\frac{1}{3}\overline{v'_i u'_i} - \frac{1}{3}\overline{v'_i v'_i}\right). \tag{20}$$

The $\frac{1}{3}\overline{v'_i u'_i}$ in the expression 20 is the modulation term and expresses the correlation of the dispersed phase fluctuations $\overline{v'}$ to the fluctuations of the carrier phase $\overline{u}'$. For droplets with high Stokes numbers St the fluctuations of the carrier phase do not interact with the droplet velocities thus the modulation term is expected to reach zero while for low inertia droplets their that follow the carrier phase fluctuations the modulation term is bounded by an upper limit $\mathcal{U}^2$.

The scope of this work is the extension of the FLA for turbulent flows by the introduction of an unresolved exchange of particles across the Lagrangian volume. The complex interaction between the dispersed phase fluctuations and the flow fluctuations of a turbulent carrier phase discussed in (81) was initially investigated by Tchen (85). In this paper, the turbulent diffusion approach has been followed for the evaluation of the turbulent mass flux in Equation 16. According to (96) the algebraic (local equilibrium) models (18, 12, 10) have gained wide acceptance for the calculation of the dispersed phase turbulent characteristics. Within the framework of one of these approaches, the turbulent stresses of the dispersed phase are directly related to the Reynolds stresses of the carrier flow. Following Danon et al. (18) we can write:

$$\frac{1}{3}\overline{v'_i u'_i} = \mathcal{U}^2 e^{-B\tau_d/\tau_t}. \tag{21}$$

Hence,

$$\frac{d\mathcal{V}^2}{dt} = \frac{2}{\tau_d}\left(\mathcal{U}^2 e^{-B\frac{\tau_d}{\tau_t}} - \mathcal{V}^2\right), \tag{22}$$

where $\tau_t$ is the characteristic turbulence time. $B$ is an empirical constant introduced in Danon et al. (18) for the round jet configuration. Following (11), where local isotropy is assumed, the empirical constant $B$ is taken equal to 0.5 (see Chan et al. (9), Pakhomov and Terekhov (58)). Equation (22) provides the rate of change of the droplet fluctuation intensity accounting for the dynamic response of droplets to the carrier phase turbulent fluctuations. Taking into account that the integral length scale is responsible for the diffusion of the discrete phase, the diffusion coefficient in (19) can be modelled on the integral length scales using $\mathcal{L} = \Delta$ and $\mathcal{V} = \lambda\mathcal{U}$, as:

$$D_T = \lambda\left(\frac{2}{3}k_{\mathrm{sgs}}\right)^{1/2}\Delta\ . \tag{23}$$

In our analysis, the standard closure for the subgrid turbulent kinetic energy has been chosen based on the magnitude of the resolved rate of the strain tensor $|\overline{S}| = \sqrt{2\overline{S}_{ij}\overline{S}_{ij}}$:

$$k_{\mathrm{sgs}} = \frac{c_S^4}{c_v^2}\Delta^2|\overline{S}|^2\ , \tag{24}$$

where $c_S$ is the Smagorinsky constant and $c_v$ is assumed to be equal to 0.1 (see Pope (66)). $\Delta$ is the length scale inferred from the size of the filtering volume $\Omega_i$, $\Delta = \Omega_i^{1/3}$, providing a measure of the resolved integral length scale. The theoretical value for the Smagorinsky constant, $C_S = 0.16$, is used in our analysis (see Lilly (44), Clark et al. (15), Kwak et al. (41)).

Integrating (16) over time and taking into account (19) we obtain the following expression for the droplet number density:

$$n_d(\mathbf{x}_0, t) = \frac{n_d(\mathbf{x}_0, 0) + \int_{\tau=0}^{\tau=t}\|\mathbf{J}(\mathbf{x}_0, \tau)\|\,\nabla\cdot\left(D_T\nabla n_d\left(\mathbf{x}_0, \tau\right)\right)d\tau)}{\|\mathbf{J}(\mathbf{x}_0, t)\|}\ . \tag{25}$$

This equation can be used for the calculation of the droplet number density for a turbulent flow field. The introduction of the concept of turbulent diffusion in FLA requires the calculation of the Laplacian of the filtered droplet number density. The calculation of the spatial derivatives for the droplet number densities is performed by projecting the FLA solution on the Eulerian mesh, resulting in a hybrid Lagrangian-Eulerian approach to the problem. The Laplacian is then calculated using a central differencing scheme.

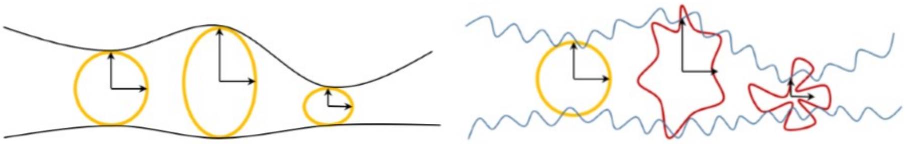

Figure 1: **Left:** Schematic pattern of the evolution of a droplet cloud element within a filtered flow field. **Right:** Schematic pattern of the evolution of a droplet cloud element within a turbulent flow field.

.

### 3.2. *Droplets in a one-dimensional standing wave.*

To illustrate the applicability of the approximations on which the model described in the previous section was based, we consider droplet dynamics in a one-dimensional oscillating flow (standing wave) with an imposed high-frequency modulation, similar to Knudt's well-known dusty-gas flow in a tube. Fundamental flow fields, which can be expressed analytically, are widely used for the study of particle clustering as presented by Monchaux et al. (53). A wide range of synthetic flows for both compressible and incompressible configurations, used for the investigation of pattern formation and clustering of particles in turbulent flows, is presented by Gustavsson and Mehlig (33).

We assume that a large number of droplets is suspended in an infinite vertical column of air. The contribution of gravity is ignored. The droplets are initially confined within a segment with length $4L$. Introducing the dimensionless distance $x$, normalised by $L$, we can write that this segment is confined between $x = -2$, and $x = 2$. We consider the case when a standing wave consisting of two harmonics is sustained within the one-dimensional column. Taking $U_m$ as the velocity scale, the dimensionless velocity of the carrier phase $u$ is presented as:

$$u(x,t) = \sum_{i=1}^{2} U_{mi} \sin(\omega_i \pi t) \sin(k_i \pi x) \ , \tag{26}$$

where $k_i$ is the wavenumber and $\omega_i$ is the angular frequency of the standing wave assumed to be proportional to the wavenumber for both harmonics ($\omega_i = 0.1k_i$); the velocity amplitude for the first harmonic is $U_{m1} = 1$, while for the second one $U_{m2} = 1/k_2$. The fundamental wavenumber $k_1$ is taken equal to unity, and the wavenumber for the modulation wave is $k_2 = 16$.

For Stokes droplets, the time evolution of their trajectories $x$, nondimensionalised by $U_m$ and $L$, is described by the following equation:

$$\ddot{x}_d + \frac{1}{\mathrm{St}}\dot{x}_d + \frac{1}{\mathrm{St}}u(x,t) = 0 \ , \tag{27}$$

where the droplet Stokes number (St) is defined as the ratio $\tau_d/\tau_v$, $\tau_v = L/U_m$.

For the carrier phase flow field described by (26), the trajectories of the droplets were calculated numerically by integrating Equation (27) for $N$ droplets. The results of calculations for $N = 10^6$ and $\mathrm{St} = 5$ are presented in Figure 2, where a representative subset of one hundred trajectories is shown. For these specific conditions the droplets show a diffusive behaviour akin to the turbulent diffusion expected in a fully turbulent flow field. The droplets oscillate and jump across the nodes of the standing wave, dispersing over time across the air column. A similar behaviour can be inferred from the plots showing the time evolution of droplet number density presented in Figure 3. As one can see from the latter figure, in addition to the turbulent mixing behaviour, the droplets form clusters (i.e. they accumulate), demonstrating un-mixing behaviour. This behaviour illustrates how mixing and un-mixing of droplets can co-exist in a single system. The fluctuations cause not only the dispersion of the droplets but also lead to formation of droplet clusters, the distance between which mimics the integral length scale of the carrier phase $L$. This 1D flow of the carrier phase is compressible but gas density variations are smooth, without shock waves. For very low-inertia droplets (St is close to zero), the droplet number densities are assumed to vary smoothly. Intersections of droplet trajectories (and formation of caustics) are expected to appear only for certain non-zero St. Hence, compressibility of the carrier phase is not important in our analysis since it does not initiate the formation of caustics. Note that the onset of local compression and dilation zones in the carrier phase in some cases may result in the onset of an additional force in the averaged momentum equation for the dispersed phase, identified as spurious drift in (69).

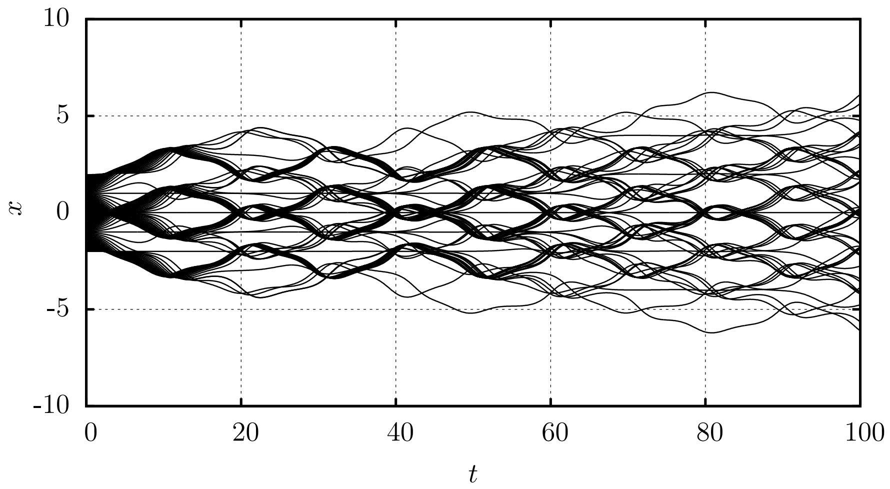

Figure 2: Trajectories of individual droplets, $x_d(t)$, dispersing due to the carrier phase velocity oscillations.

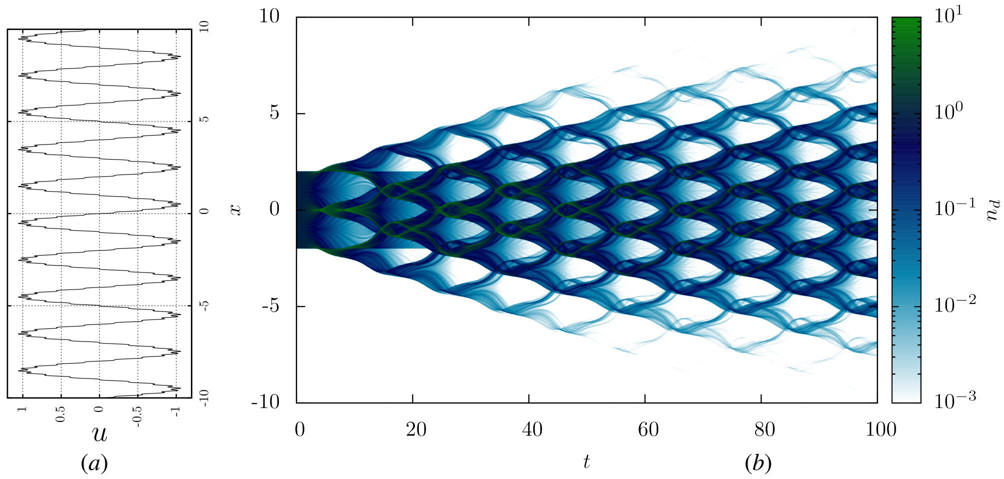

Figure 3: **Left:** Distribution of the carrier phase $u(x, t)$ velocity for the one-dimensional Knudt's tube problem, taking into account the contribution of 2 harmonics, at $t = 5$. **Right:** Number density $n_d$ distribution across Knudt's tube over time for droplets dispersing due to carrier phase velocity oscillations.

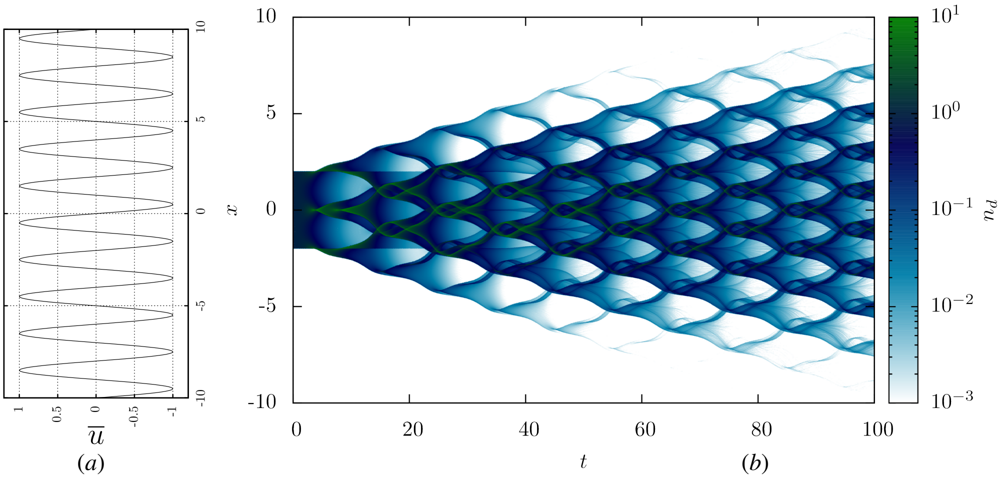

Figure 4: **Left:** Distribution of the carrier phase $u(x, t)$ velocity for the one-dimensional Knudt's tube problem, taking into account the contribution of 1 harmonic, at $t = 5$. **Right:** Number density $n_d$ distribution across Knudt's tube over time for droplets dispersing due to carrier phase velocity oscillations.

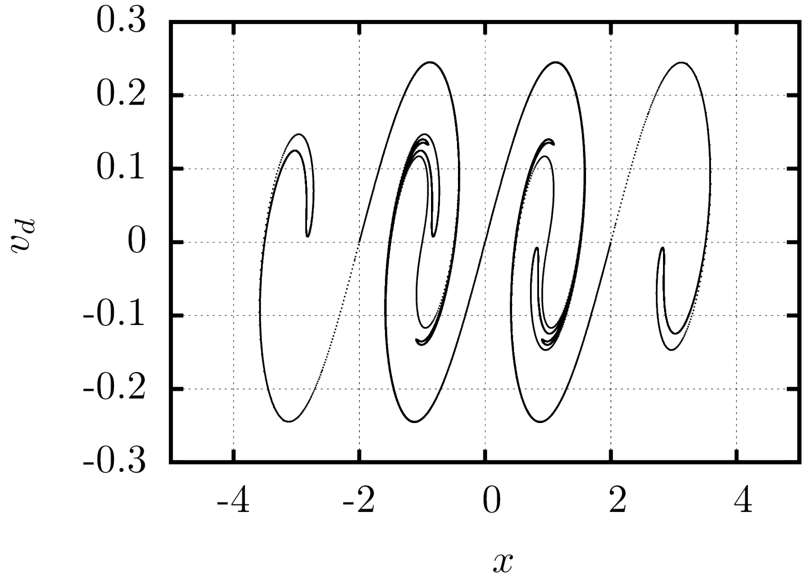

Figure 5: The velocity distribution of the droplets dispersing in Knudt's tube at $t = 20$; multiple folds in droplet trajectories can be clearly seen.

Let us now consider the droplet dynamics in a single standing wave in a gas flow:

$$\overline{u}(x,t) = U_{m1}\sin(\omega_1 \pi t)\sin(k_1 \pi x) \ . \tag{28}$$

In what follows we refer to the velocity distribution (28) as the filtered carrier phase flow field.

In Figure 4 the same plots as in Figure 3, but for the case when the standing wave is approximated only by the first harmonic, are presented. Comparing Figure 3 and Figure 4, in both cases (1 and 2 harmonics) we can observe the mixing and un-mixing behaviour of droplets. At the same time, the filtering leads to the smoothing of the wrinkles in the number density induced by the modulation wave compared with the number density distribution in the un-filtered gas flow (2 harmonics). Note that the trajectories shown in Figure 2 for the un-filtered gas flow are almost indistinguishable from those inferred from the filtered gas flow (not shown in the paper).

The velocities of the droplets for $t = 20$ for the un-filtered (two harmonics) flow are shown in Figure 5. As can be seen from this figure, the droplet trajectories overlap at some values of $x$, leading to multiple velocities for each $x$. These overlapping layers can be identified by droplet velocities or their Lagrangian coordinate $x_0$.

In Figures 6(a) and 6(b), the droplet number densities inferred from the FLA, are compared with the number densities inferred from counting the numbers of droplets across 1000 bins (see Figure 3 and 4) for filtered (Figures 6(a)) and un-filtered (Figures 6(b)) carrier phase flows. In the FLA, the number density for each layer is calculated based on continuity equation (6).

In the FLA framework, the droplet number densities in an infinitesimal Eulerian volume $n_d$ are inferred from the Lagrangian number densities. This is achieved by adding the averaged Lagrangian values of the latter for each fold in the droplet cloud found within this volume. This process requires rigorous identification of the folds. This identification is based on a suitably chosen conditioning variable $c$ which can be the droplet velocity, the initial Lagrangian position or the number of changes of the sign of the Jacobian determinant. Conditioning the number density by $c$, i.e. $\langle n_d | c \rangle$ gives the average number density at each fold, while the following integral gives the final value of the number density as predicted by FLA:

$$n_d^T = \int_{-\infty}^{\infty} \langle n_d | c \rangle \sum_{i}^{N_{\text{folds}}} (\delta(c - c_i)) dc \ , \tag{29}$$

where, $c_i$ is the value of the conditioning variable at each fold, and $\delta$ is the Dirac delta function.

The initial Lagrangian position $x_0$ is used as the conditioning variable $c$. The number densities for each layer, shown as dashed curves in Figure 6, are summed up. This leads to the total number density inferred from the FLA, shown as circles in the same figure. Four well identified regions where intersection of trajectories occurs can be clearly seen in this figure. In these regions, folds of the dispersed phase are formed resulting in caustic points where droplets accumulate. Here the droplet number densities become very high. This can be clearly predicted by the FLA. In the vicinity of the folds, the results inferred from the FLA, are not close to those inferred from counting the number of droplets at each bin. Although the number densities at caustic points (where the Jacobian is crossing zero) tend to infinity, they are integrable (56). This leads to finite number densities for the specific intervals (bins). For the approach based on box counting of droplets a significant number of individual droplets is needed to achieve accurate estimation of the number densities at the caustic points.

Comparing the plots shown in Figures 6(a) and 6(b), one can see that the number densities predicted for the un-filtered carrier phase flow are much more chaotic than those predicted for the filtered flow. Let us now recall that the analysis presented in Section 3 is valid only when the ratio $|\mathbf{j}_T|/(n_d|\overline{\mathbf{v_d}}|)$ (normalised turbulent mass flux $\hat{j}_T$) is much greater than the ratio $\overline{v'_{d,i}v'_{d,j}}/\overline{v}_{d,i}^2$ (normalised turbulent momentum flux (pressure) $\hat{p}_T$). It is not possible to prove the validity of this condition in the general case. In what follows, however, we will show that it is valid in the case of droplet dynamics in the un-filtered carrier phase flow (two harmonics) when the filtered flow (one harmonic) is considered as a base flow.

The values of $\hat{j}_T$ and $\hat{p}_T$ were calculated based on the following general expressions:

$$\hat{j}_T = \left| |\widetilde{n_d v_d}| - |\widetilde{\overline{n}_d \overline{v}_d}| \right| / |\widetilde{n_d \overline{v}_d}| \ , \tag{30}$$

$$\hat{p}_T = \left| \widetilde{n_d v_d^2} - \widetilde{\overline{n}_d \overline{v}_d^2} \right| / \widetilde{n_d \overline{v}_d^2} \ , \tag{31}$$

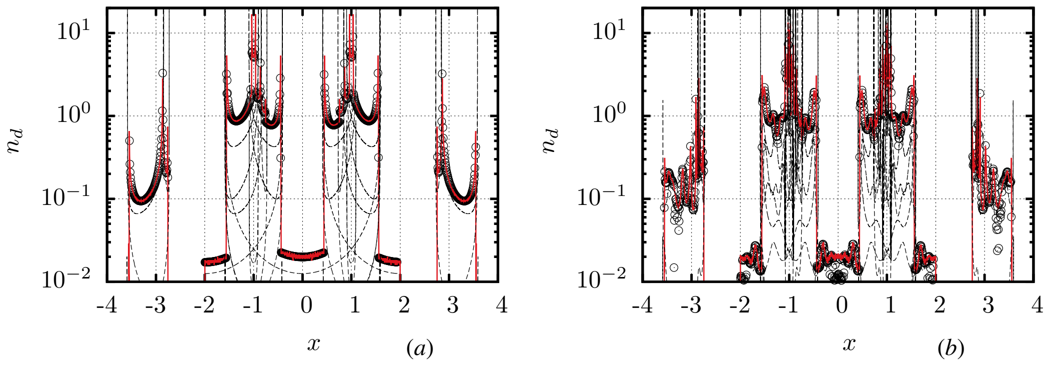

(*a*) (*b*)

Figure 6: Droplet number density distributions at $t = 20$. Solid red curve: number density calculated by spatially averaging the number of individual droplets across 1000 bins at specific points along the $x$−axis. Dashed curves: inverse of the determinant of the Jacobi matrix showing the droplet number density at each fold. Circles: number densities obtained by summing up the number densities at each fold. **Left:** Filtered carrier phase velocity field (one harmonic). **Right:** Un-filtered carrier phase velocity field (two harmonics).

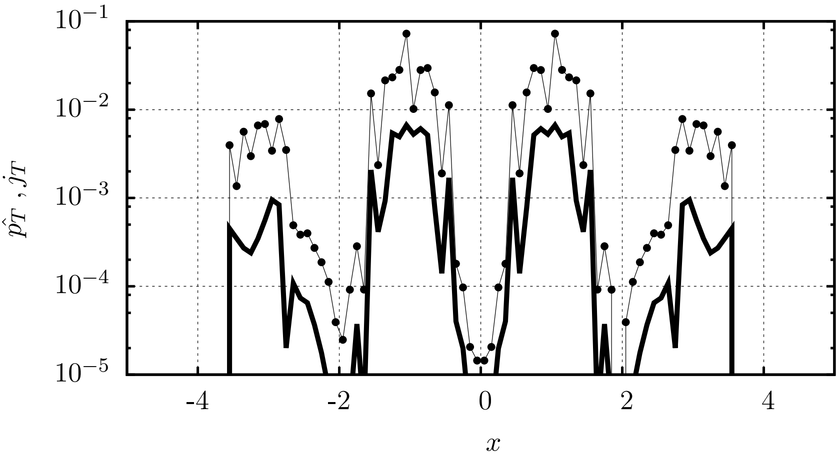

Figure 7: Turbulent momentum flux (pressure), normalised by the resolved momentum flux $n_d\overline{v}_d^2$ ($\hat{p}_T$) (thick solid curve), and the turbulent mass flux, normalised over the resolved mass flux $n_d\overline{v_d}$ ($\hat{j}_T$) (thin solid curve with symbols •) at time $t = 20$ for the droplets dispersing in the un-filtered (2 harmonics) flow in Knud's one-dimensional tube problem. The filtered (one harmonic) flow is considered as the base flow.

where operator $\widetilde{\cdot}$ shows averaging over the control volume that corresponds to the wavelength of the second harmonic. The filtering operator $\bar{\cdot}$ for the droplet velocity $v_d$ and the number density $n_d$ show the values inferred from the filtered carrier phase velocity field.

The plots of $\hat{j}_T$ and $\hat{p}_T$ versus $x$ are shown in Figure 7. As can be seen from this figure, $\hat{p}_T$ is generally much (up to about an order of magnitude) smaller than $\hat{j}_T$ (the cases when both these terms are equal to zero are of no interest to us) (cf. (2)). This illustrates (but does not prove) the applicability of the condition $\hat{j}_T \gg \hat{p}_T$ used in our analysis.

## 4. The filtered number density and a second order extension of the FLA

In the previous section we presented the formulation of the effect of turbulent diffusion on droplet dispersion in the FLA framework. We demonstrated the implementation of the FLA in an unsteady one-dimensional flow-field and assessed the modelling assumptions for the conservation of mass and momentum. To introduce the FLA in the LES framework, however, the point-wise number density needs to be related to the finite length scale inferred from the LES filter width $\Delta$.

In this section we present the second order extension of the FLA showing the spatial structure of the number density field (62). Most importantly the following analysis describes how the FLA approach can model the detailed structure of caustic formations. This is achieved by introducing the second order approximation of the dispersed continuum deformation, the calculation of the filtered number density and finally by the calculation of the Hessian of the transformation of the continuum space in the FLA context.

### *4.1. The number density in a finite volume*

We consider a one-dimensional Stokesian droplet continuum at the locations $x$ at times $t$ which corresponds to its initial distribution at locations $x_0$ which span from $x_0 = 0$ to $x_0 = 1$ at time $t = 0$ as shown in Figure 8. This continuum disperses and deforms as shown by the solid curve in Figure 8. Function $x(x_0)$ is uniquely defined at $x_0$. The filtered number density at any point $C$ is obtained by spatially averaging the number of droplets within a filtering volume of size $\Delta$ on the $x$ axis. We can define the local coordinate system $\delta = x_0 - x_0^C$ and $\epsilon = x - x^C$ for the distribution of the deformed continuum. The point-wise number density $n_d$ at a point $\epsilon_0$ in the local coordinate system is calculated as:

$$n_d(\epsilon_0) = \left|\lim_{\epsilon\to\epsilon_0} \frac{\delta(\epsilon) - \delta(-\epsilon)}{2\epsilon}\right| = \left|\frac{\partial\delta}{\partial\epsilon}\right|_{\epsilon=\epsilon_0}, \tag{32}$$

where $\frac{\partial\epsilon}{\partial\delta}$ is equal to the Jacobian $J$ and $n_d = 1/|\mathbf{J}|$. Equation 32 can be inferred from the mass conservation 3. If $C$ is located at a caustic point, where $\frac{\partial\epsilon}{\partial\delta}$ is zero, then the number density at $C$ is infinitely large. It will be shown later in this section that the number density distribution can be integrable over a finite volume, and a filtered number density $\hat{n}_d$ can be defined and predicted.

Assuming that the number density $\frac{\partial\delta}{\partial\epsilon}$ is integrable in the interval $\epsilon_0 \in [-R_\epsilon, R_\epsilon]$, the spatially averaged or filtered number density $\hat{n}_d$ for an interval $\Delta = 2R_\epsilon$ of the Eulerian space $\epsilon$ can be estimated as:

$$\hat{n}_d = \frac{1}{2R_\epsilon}\int_{-R_\epsilon}^{R_\epsilon} n_d d\epsilon = \left|\frac{\delta(\epsilon = R_\epsilon) - \delta(\epsilon = -R_\epsilon)}{2R_\epsilon}\right|, \tag{33}$$

where $n_d$ is evaluated from Equation 32. For the first order FLA, a simple linear expression for the dispersed continuum distribution $\epsilon = J\delta$ is assumed. In this case, Equation 33 leads to the standard first order expression for the filtered number density $\hat{n}_d = 1/J$. As shown in Figure 8, in the vicinity of a fold the linear approximation for $\epsilon(\delta)$ cannot represent the topology of the fold. We introduce the second order Taylor approximation for $\epsilon(\delta)$ as:

$$\epsilon(\delta) = \left.\frac{\partial\epsilon}{\partial\delta}\right|_{\delta=0}\delta + \frac{1}{2}\left.\frac{\partial^2\epsilon}{\partial\delta^2}\right|_{\delta=0}\delta^2. \tag{34}$$

The first derivative $\frac{\partial\epsilon}{\partial\delta} = \frac{\partial x}{\partial x_0}$ in Expression 34 is equal to the Jacobian $J$, while the second derivative $\frac{\partial^2\epsilon}{\partial\delta^2} = \frac{\partial^2 x}{\partial x_0^2}$ is equal to the Hessian $H$ of the transformation from the Eulerian $x$ to the Lagrangian coordinate $x_0$ at the point $\epsilon = 0$. Thus, the approximation of the transformation $\epsilon(\delta)$ (dashed parabola in Figure 8 **Left**) can be presented as:

$$\epsilon(\delta) = J\delta + \frac{1}{2}H\delta^2. \tag{35}$$

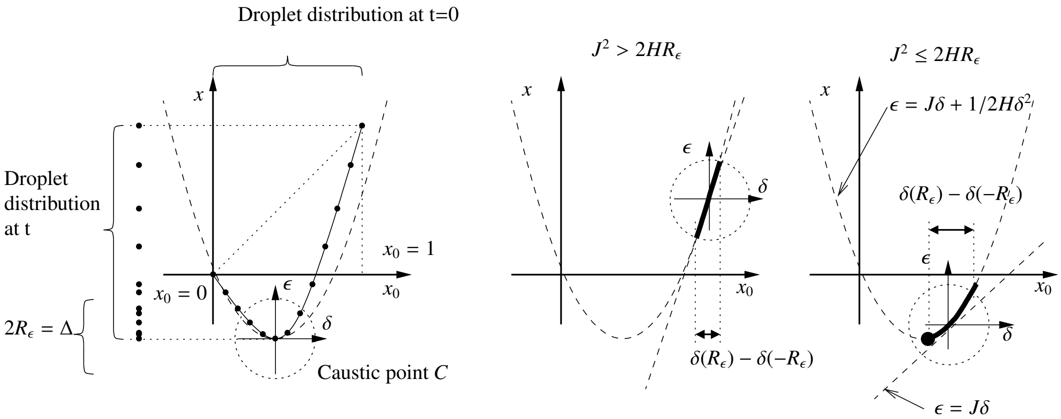

Figure 8: **Left:** Schematic representation of the deformation of the dispersed continuum at the vicinity of a fold. The horizontal axis represents the initial Lagrangian coordinate $x_0$. The vertical axis corresponds to the current Eulerian coordinate $x$ at time $t$. Straight dotted line: the distribution $x(x_0)$ for $t = 0$. Solid curve: the distribution $x(x_0)$ at time $t$. Dashed curve: the approximation of the continuum distribution in the second order FLA. Axes $\delta$ and $\epsilon$ correspond to the local coordinate system at $C$. **Middle:** The position of the filtering interval $\Delta = 2R_\epsilon$ around $C$ when $J^2 > 2R_\epsilon H$. **Right:** The position of the filtering interval $\Delta = 2R_\epsilon$ around $C$ when $J^2 < 2R_\epsilon H$. Straight dashed line: the approximation of the continuum distribution in the first order FLA.

We can choose the orientation of the local coordinate system $\delta = \pm(x_0 - x_0^C)$ and $\epsilon = \pm(x - x^C)$ to ensure that both $H$ and $J$ are positive. The solution to (35) can be presented as:

$$\delta(\epsilon) = \frac{-J + \sqrt{J^2 + 2H\epsilon}}{H}\ , \tag{36}$$

were we have chosen the root closest to the Taylor expansion reference point. We can evaluate Expression (33) for the filtered number density as:

$$\hat{n}_d = \frac{\frac{-J+\sqrt{J^2+2HR_\epsilon}}{H} - \frac{-J+\sqrt{J^2-2HR_\epsilon}}{H}}{2R_\epsilon} = \frac{2}{\sqrt{J^2 + 2HR_\epsilon} + \sqrt{J^2 - 2HR_\epsilon}}\ , \tag{37}$$

when $J^2 > 2HR_\epsilon$. For $J^2 < 2HR_\epsilon$, Solution (36) is defined only for $\epsilon = R_\epsilon$ as for $\epsilon = -R_\epsilon$ the filtering interval extends outside the fold of the dispersed continuum. In this case the integral in Equation (33) is evaluated only in the interval $[\epsilon_{min}, R_\epsilon]$. $\epsilon_{min}$ corresponds to the minimum limit of the droplet distribution that occurs at $\delta_{min} = -J/H$. Thus, for the case when Jacobian $J$ is small relative to the curvature of the fold, the number density inferred from Equation (33) can be estimated as:

$$\hat{n}_d = \frac{\frac{-J+\sqrt{J^2+2HR_\epsilon}}{H} + \frac{J}{H}}{2R_\epsilon} = \frac{\sqrt{J^2 + 2HR_\epsilon}}{2R_\epsilon H}, \tag{38}$$

when $J^2 - 2HR_\epsilon < 0$. As follows from Equation 38, the number density for a caustic point $J = 0$ becomes:

$$\hat{n}_d = \frac{1}{\sqrt{2R_\epsilon H}}\ . \tag{39}$$

Both Equations (36) and (37) reduce to the classical FLA expression $n_d = 1/J$ for $R_\epsilon \to 0$. Thus, even if the Jacobian is zero at $C$ the number density is integrable in the vicinity of $C$ if Hessian $H$ is non-zero (Morse critical point). In the general case, the integral of the number density averaged within a volume with radius $R_\epsilon$ can be calculated as:

$$\hat{n}_d = \begin{cases} \frac{2}{\sqrt{J^2+2HR_\epsilon}+\sqrt{J^2-2HR_\epsilon}} & \text{if } J^2 - 2HR_\epsilon > 0 \\ \\ \frac{\sqrt{J^2+2HR_\epsilon}}{2R_\epsilon H} & \text{if } J^2 - 2HR_\epsilon < 0\,. \end{cases} \tag{40}$$

When $J^2 = 2HR_\epsilon$ then $\hat{n}_d = \sqrt{2}/J$ for both the first and second branches of Equation (40). For $J^2 >> 2HR_\epsilon$, where the dispersed phase is diluted, the above expression simplifies to the classical FLA expression $\hat{n}_d = 1/J$.

This model can be applied for multi-dimensional cases taking into account that the local structure of the fold is one-dimensional, i.e. the caustic is a surface in three dimensions or a curve in two dimensions. This can be supported by our findings in Section 5 (cf. Figure 17).

### *4.2. Calculation of the Hessian*

In this section, a method for calculation of the value of the Hessian along a trajectory will be presented. This method is similar to the approach used in the classical FLA for the calculation of the Jacobian. An initial value problem for the time derivative of the Hessian, represented by the auxiliary variable $\psi$, can be formulated by differentiating the equivalent expression for $\omega$ over the Lagrangian coordinate $x_0$. The derivation of the initial value problem is presented in the Appendix A. The initial value problem for the calculation of the Hessian and the Jacobian is finally described by the following explicit non-linear differential system of equations:

$$\frac{\partial}{\partial t}\begin{bmatrix} J \\ \omega \\ H \\ \psi \end{bmatrix} = \begin{bmatrix} \omega \\ \frac{1}{\tau_d}\left(\frac{\partial U}{\partial x}J - \omega\right) \\ \psi \\ \frac{1}{\tau_d}\left(\frac{\partial^2 U}{\partial x^2}J^2 + \frac{\partial U}{\partial x}H - \psi\right) \end{bmatrix}, \quad \text{with} \quad \begin{bmatrix} J \\ \omega \\ H \\ \psi \end{bmatrix}_{t=0} = \begin{bmatrix} 1 \\ \frac{\partial V}{\partial x} \\ 0 \\ \frac{\partial^2 V}{\partial x^2} \end{bmatrix} \tag{41}$$

System (41) will be solved numerically using a fourth order Runge-Kutta method. The same method can be implemented for a multi-dimensional case, where each component of the Hessian tensor $H^k_{ij} = \frac{\partial U_k}{\partial x_{0,i} x_{0,j}}$ and its equivalent auxiliary variable $\psi^k_{ij} = \frac{\partial}{\partial t}H^k_{ij}$ is integrated by the corresponding ODE.

For the results of the second order FLA presented in the next section, the differential system 41 is numerically integrated over time using a fourth order Runge-Kutta method. The same method can be implemented for a multi-dimensional case for finding each component of the Hessian tensor $H^k_{ij} = \frac{\partial x_k}{\partial x_{0,i} x_{0,j}}$ and its equivalent auxiliary variable $\psi^k_{ij} = \frac{\partial}{\partial t}H^k_{ij}$.

### *4.3. Droplets in a one-dimensional converging flow*

In this section we demonstrate the calculation of spatially filtered number density $n_d$ within a finite volume $\Delta = 2R_\epsilon$ using the second order FLA. We compare the second order FLA results with the results inferred from the standard Lagrangian approaches where the number density is calculated by a box counting method. As in the previous one-dimensional numerical simulations, we assume that a large number of droplets is suspended in an infinite vertical column of air. For the dimensionless distance $x$, normalised by $L$, the droplets are distributed between $x = -0.5$, and $x = 0.5$. We assume a simple compressible converging one-dimensional flow field $u(x)$ for the carrier phase, described by the following equation:

$$u(x,t) = -\cos(2\pi x). \tag{42}$$

The problem is modelled using a standard Lagrangian approach with $10^6$ individual droplets dispersing under the influence of the carrier phase field using Equations (1) and (2) for Stokes droplets. The Stokes number for this case is assumed equal to St= 10.0. The number density for each FLA droplet is calculated using Equation (6) for the first order FLA and Equation (40) for the second order FLA. The Jacobian and the Hessian are calculated using the fourth order Runge-Kutta method for the integration of System (41), as described in the previous section.

Under the influence of the carrier phase flow field the droplets collapse towards the centreline and undulate due to their high inertia. The trajectories of the FLA droplets are shown in Figure 9 (**Left**). The size of the droplets

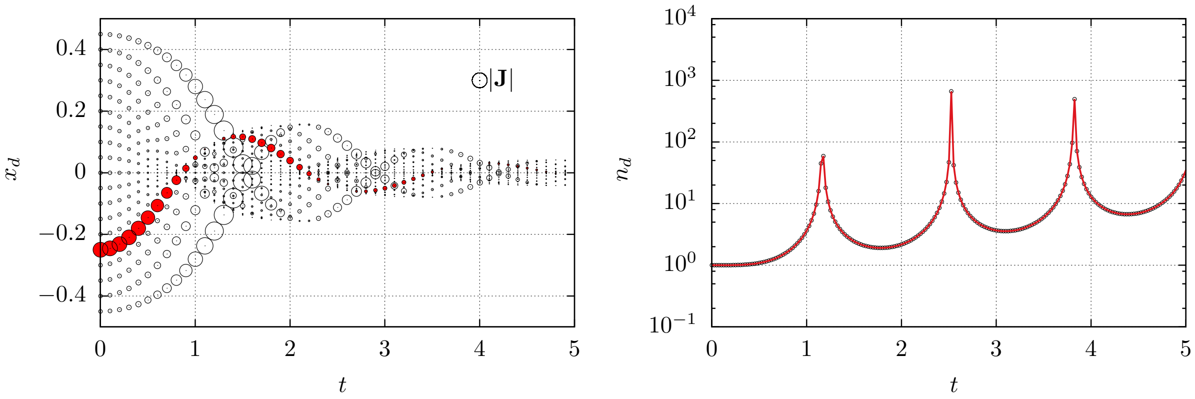

Figure 9: **Left:** Trajectories of FLA droplet clouds, $x_d(t)$, dispersing in the carrier phase. The circles diameters are proportional to the magnitude of Jacobian $J$. **Right:** Number density $\hat{n}_d$ on a single fold along the $x_0 = -0.25$ droplet trajectory assuming an infinitesimally small averaging volume with $R_\epsilon \to 0$.

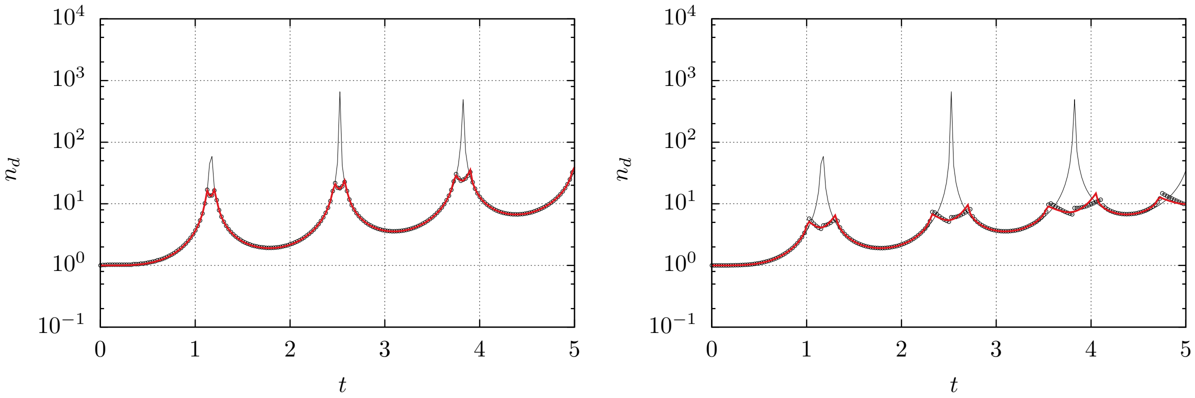

Figure 10: **Left:** Number density $\hat{n}_d$ on a single fold along the $x_0 = -0.25$ droplet trajectory, assuming an averaging volume with $2R_\epsilon = 0.001$. **Right:** Number density $\hat{n}_d$ along the $x_0 = -0.25$ droplet trajectory assuming an averaging volume with $2R_\epsilon = 0.01$. Solid red curve: result from the second order FLA. Circles: result from box counting on the same length scale. Thin curve: result from the standard FLA.

is proportional to the magnitude of Jacobian $J$. Small circles indicate high number densities. The Jacobian is zero at the locations where the carrier phase field compresses droplet clouds, resulting in trajectory intersections. The number density of the droplet gradually increases with time as droplets converge into a progressively smaller space. The droplet trajectory $x_0 = -0.25$ highlighted in Figure 9 (**Right**) will be used as a reference trajectory for the presentation of the first and second order FLA results.

In Figure 9 (**Right**) we present the comparison of number densities along a single trajectory using the standard FLA method (or assuming $R_\epsilon = 0$). The result for a single FLA droplet is compared with the result inferred from the box counting Lagrangian method where the minimal box size containing three droplets is used. As can be seen from this figure, the standard FLA approach allows us to predict adequately the droplet number density using a single Lagrangian element. It can be observed, however, that the number densities at the vicinity of the trajectory intersections (at $t = 1.2$ for the $x_0 = -0.25$) reach very high values. The values of these densities vary depending on the number of droplets used and the temporal resolution and can become infinitely large. In the first order FLA context, the structure of the droplet distribution close to caustics is considered as unresolved at a finite length scale.

In Figure 10 we show the values of the number density as inferred from the second order FLA. In Figure 10 (**Left**) we show the number density for a filter width equal to $R_\epsilon = 0.0005$, as compared with the predictions of the standard FLA and the box counting method. The latter uses $N = 10^6$ droplets, assuming an averaging volume $\Delta$ of the same size.

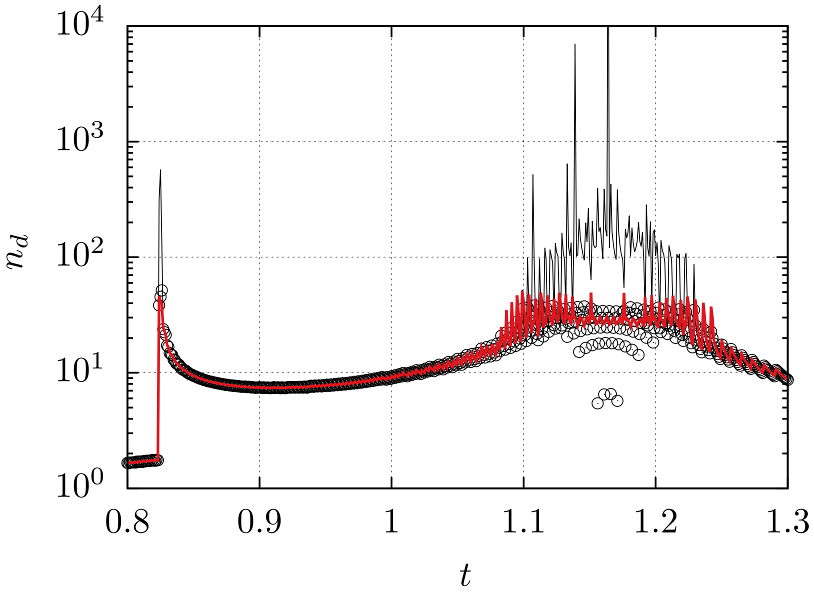

Figure 11: Total number density $\hat{n}_d$ along the $x_0 = -0.25$ droplet trajectory assuming an averaging volume with $2R_\epsilon = 0.001$. Solid red curve: result inferred from the second order FLA. Circles: result inferred from box counting on the same length scale. Thin curve: result inferred from the standard FLA.

As can be seen from the figures above, the description of the inner structure of the caustic formations in the second order FLA context results in the accurate prediction of the filtered number density calculated by the box counting Lagrangian simulation. Given that in the vicinity of the trajectory intersections the Hessian of the dispersed continuum distribution is finite, the second order FLA not only results in a finite value for $n_d$, but also provides an accurate prediction of the values of the filtered number density $\hat{n}_d$ (see Appendix B). Of course, in the regions away from caustic formations, the dispersed continuum structure is resolved, and both the standard FLA and the second order FLA give the same predictions. As can be seen in the same Figure 10 (**Right**), the box counting method shows a discontinuity at the trajectory intersection. This is not observed for the result inferred from the second order FLA. The reason for this behaviour is that the branch of the upwind fold is not symmetric relative to the branch of the downwind fold. This could be modelled by introducing the third order approximation for the distribution of the dispersed continuum. In the immediate vicinity of the caustic, the filtering volume is only partly occupied by droplets. This explains the decrease in the droplet number density observed on the caustic, as shown in the same figure.

The total number density, calculated for all the trajectories from every fold found within a volume of characteristic length $\Delta$ along the path of the $x_0 = -0.25$ droplet, is shown in Figure 11. In order to obtain the total average number density, the domain $-0.5L$ to $0.5L$ is divided into finite volumes of size $\Delta$. For the direct simulation using Lagrangian droplets we count all the droplets within the averaging volume in which the reference droplet is found. The summation of the folds for the standard and the second order FLA approaches is also performed for the same volumes using Equation 29. In Figure 11 we focus on the time interval $t = 0.8$ to $t = 1.3$. In this interval, we observe two regions of high number density. The first consists of a single peak at $t = 0.825$ which coincides with the intersection of the reference trajectory with distant trajectories which have formed a caustic. The peak at this point reaches $n_d = 40$ as predicted by the second order FLA and the box counting method. The standard FLA provides a spurious (non-converging) prediction of $n_d = 500$. After this peak, the number density remains almost constant with $n_d \sim 10$. The second region consists of a series of peaks and coincides with the folding of the reference trajectory itself. In both cases, the second order FLA predicts the filtered number density by modelling the internal structure of the dispersed continuum fold. For the specific filter length $\Delta = 0.001$ used in Figure 11, the second order FLA shows peaks of number density that are only 2 to 3 times the number densities away from caustics. This agrees with the direct simulation result.

Note that the standard FLA approach accurately predicts the occurrence of the formation of caustics, as will be discussed in Section 5, while the second order approach provides a spatially filtered value. The box counting method needs a very large number of droplets to identify the details of the internal structure of the fold even for simple one-or two-dimensional problems. For three-dimensional and/or more complicated problems, a simple Lagrangian approach would require a prohibitive number of droplets for the description of caustics.

## 5. Droplet mixing in homogeneous and isotropic turbulence

In this section, the model is applied to the analysis of time evolution of the localised droplet distribution in the field of decaying homogeneous and isotropic turbulence of the carrier phase. The Lagrangian approach is used to show the structure of the dispersed phase distribution under the influence of a complex turbulent flow field characterised by detailed simulations with an order of $10^8$ degrees of freedom. The Lagrangian methods based on the statistical properties of a large number of droplets would require a computationally prohibitive number of individual droplets (as demonstrated in the simple one-dimensional fields) to resolve the complex fine scale of the dispersed continuum structure. Thus, statistical analysis of simple Lagrangian droplets for this family of problems is used only for the assessment of the turbulent diffusion problem.

### *5.1. Numerical method: The solution and the initialisation of the carrier phase DNS*

The turbulent mixing of droplets is investigated using numerical experiments on homogeneous and isotropic turbulence. The evolution of the turbulent flow field is governed by the incompressible Navier-Stokes (NS) equations. The solution for the turbulent flow field is inferred from the numerical integration of the NS equations for the vorticity $\omega = \nabla \times \mathbf{U}$:

$$\frac{\partial \mathbf{U}}{\partial t} = \mathbf{U} \times \omega - \nabla \Pi + \frac{1}{\mathrm{Re}} \nabla^2 \mathbf{U} \, , \tag{43}$$

$$\nabla^2 \Pi = \nabla (\mathbf{U} \times \omega) \, , \tag{44}$$

where Re is the Reynolds number (all variables in this section are dimensionless) and $\Pi$ is the total pressure:

$$\Pi = p + \frac{1}{2} |\mathbf{U}|^2 . \tag{45}$$

Equation (43) is solved using the pseudo-spectral method derived by Rogallo (73) in its parallel implementation as described by Papoutsakis (61). This code is based on the code originally developed by Kerr (40).

The computational domain, used in our analysis, is a cube with size $L = 2\pi$ with periodic boundary conditions in all three directions. Equation (43) is integrated in the spectral space. It is necessary to calculate the non-linear term $\mathbf{U} \times \omega$ in the physical space. One Real Fast Fourier Transform (RFFT) and two Complex FFTs (CFFT) are applied in order to obtain $\mathbf{U} \times \omega$ in the spectral space. The alias errors occurring during the Fourier transformations are removed using the $2/3$ rule (the high wavenumber part of the spectrum is ignored) Kerr (40). The initial value problem described by Eqs. (43) and (44) is integrated over time using the minimal storage time-advancement third order Runge-Kutta scheme developed by Alan Wray as described in Kerr (40). In this algorithm, three realisations of the flow field at three equivalent intermediate time steps are used to provide the final prediction.

Simulations of turbulent flow fields are based on taking into account all the scales of turbulent fluctuations. One of the conditions for the full resolution of a turbulent flow field stems from the requirement that the dissipation spectrum must be resolved. For any pseudospectral implementation, this restriction is described as Pope (66):

$$\Delta x < \frac{2\pi}{3} \eta \, , \tag{46}$$

where $\Delta x = 2\pi / N_{\mathrm{DNS}}$ is the spatial resolution of the solution.

The initial conditions for the homogeneous isotropic turbulence calculations are artificially composed using synthetic turbulence. Following the spectral reconstruction method Kerr (40), the initial flow field is considered as the

| | | | |
|---|---|---|---|
| Number of nodes | $N$ | $256^3$ | |
| Spatial resolution | $\Delta x$ | 0.025 | |
| Reynolds number | Re | 200 | |
| | | $t = 0$ | $t = 2$ |
| Turbulent kinetic energy | $k_t$ | 1.57 | 0.66 |
| Kolmogorov length scale | $\eta$ | 0.0214 | 0.0257 |
| Kolmogorov time scale | $\tau_\eta$ | 0.0922 | 0.1325 |
| Taylor microscale | $\lambda_T$ | 0.366 | 0.314 |
| Taylor Reynolds number | $\mathrm{Re}_T$ | 74.8 | 45.4 |
| Integral length scale | $\mathcal{L}$ | 1.03 | 0.95 |
| Integral time scale | $\tau_t$ | 1.02 | 1.43 |
| Integral Reynolds number | $\mathrm{Re}_l$ | 211 | 127 |

Table 1: Non-dimensional parameters for the Direct Numerical Simulation of homogeneous and isotropic turbulence, at $t = 0$ and at $t = 2$.

superposition of Fourier modes. The intensity of each Fourier mode is initialised using the energy spectrum $E(|\mathbf{k}|)$ provided by Orszag and Patterson (55):

$$E(|\mathbf{k}|) = c|\mathbf{k}|^4 e^{-|\mathbf{k}|^2/a^2} \, , \tag{47}$$

where $\mathbf{k}$ is the wavenumber vector for each mode. Constants $c$ and $a$ are chosen in such a way that all scales of the resulting turbulent flow field are well resolved (see Mell et al. (50)). The phases for each of the Fourier modes are chosen randomly, subject to consistency with the mass conservation equation (see Hussaini and Zang (37)). The synthetic turbulent flow field stemming from (47) does not have a developed dissipation spectrum and does not lead to correct high order velocity correlations (see Kerr (40)).

In order to obtain a homogeneous isotropic turbulent flow field, the initial synthetic field is integrated over time, while the energy of the large eddies is maintained by forcing. Forcing mimics the energy cascade from larger to smaller scales observed in turbulent flows. This maintains the kinetic energy of the turbulent flow field during its integration and avoids its decay due to viscosity. In the current implementation, the forcing is achieved by artificially increasing the energy of the fluctuations for the two lowest wavenumbers with $|\mathbf{k}| = 1$ and $|\mathbf{k}| = 2$ when the total turbulent kinetic energy becomes smaller than its initial value. This forcing is applied until the turbulence statistics of the flow converge to a constant value. At this stage a developed turbulent flow field was obtained and used as an initial condition for the numerical experiments of droplet dispersion.

The details of the calculated turbulent flow field are summarised in Table 1. Mesh resolution of $N = 256^3$ nodes was used. This allows adequate resolution of the dissipation spectra of the simulations of homogeneous and isotropic turbulence. The resulting flow field is characterised by a Reynolds number (based on the Taylor microscale $\lambda_T$ and the characteristic velocity $\mathcal{U}$) equal to $\mathrm{Re}_T = 74.8$. The definition of the Taylor microscale is based on the two point velocity correlation coefficient. It is calculated from the carrier phase turbulent kinetic energy $(3/2)\mathcal{U}^2$ and the dissipation rate $\epsilon$ as:

$$\lambda_T = \sqrt{15\nu\frac{\mathcal{U}^2}{\epsilon}} \, , \tag{48}$$

where $\mathcal{U}^2$ and $\epsilon$ were evaluated from the DNS data.

### 5.2. Numerical method: The solution and the initialisation of the dispersed phase

The dispersed phase is modelled by a statistically significant number $N_d$ of sampling droplets. Initially, the droplets are uniformly distributed across the cubic computational domain. Their trajectories are calculated by integrating the initial value problem (9), using the same minimal storage time-advancement third order Runge-Kutta scheme as for the integration of the flow field. Droplet acceleration due to the drag induced by the turbulent flow field is calculated from (14). For the Fully Lagrangian Approach (FLA) calculations, the elements of the Jacobian matrix and the corresponding auxiliary variable matrix are also obtained using (10) and (11) for each sampling droplet. The corresponding equations are solved using the same third order Runge-Kutta scheme. The interactions between droplets and the effect of droplets on the carrier phase are ignored assuming low mass load of the dispersed phase.

During the first stages of the numerical experiment, the droplets are expected to adapt to the fluctuations of the carrier phase flow field. To reduce this adaptation stage, droplet velocities are initialised by the asymptotic values given by (22):

$$V_i\,(t=0) = e^{\frac{1}{2}\left(-B\frac{\tau_d}{\tau_t}\right)} U_i\,(t=0)\ . \tag{49}$$

Following Lebedeva et al. (43), the elements of the Jacobi matrix $J_{ij}$ and matrix $\omega_{ij}$ in (10) and (11) are initialised as:

$$J_{ij}\,(t=0) = \delta_{ij}\ ,\ \ \omega_{ij}\,(t=0) = \frac{\partial V_i}{\partial x_j}\ , \tag{50}$$

where $\delta_{ij}$ is the Kronecker delta.

To verify the predictions of the model we compared the filtered number densities of droplets, inferred from the exact DNS solution, and the number densities for sampling droplets inferred from our model, using the filtered DNS solution.

The topology of the numerical experiments is presented in Figure 12. The computational domain with size $L = 2\pi$ is divided into $N_{\mathrm{LES}}^3$ volumes with filter width equal to $\Delta = \frac{2\pi}{N_{\mathrm{LES}}}$. The DNS solution $\mathbf{U}(\mathbf{x}, t)$ is filtered in space using the box filtering operator $\bar{\cdot}$ described by (13). Thus, the filtered flow field $\overline{\mathbf{U}}(\mathbf{x}, \mathbf{t})$ is obtained.

The test case used as a benchmark for our investigation is the diffusion of droplets initially arranged in a slab formation as shown in Figure 12. A uniform distribution of sample droplets was assumed, with the droplets scattered across the computational domain. The diffusion of droplets to the areas away from the initial concentration of droplets is considered. The sample droplets within the slab region were initialised with number density $n_d = 1$, whereas the sample droplets in the areas where the number density of individual droplets is zero are initialised with $n_d = 0$. This initialisation is summarised as:

$$n_d(\mathbf{x}, \mathbf{0}) = \begin{cases} 1, & \text{if } |x_3 - \pi| \leq \pi/2 \\ 0, & \text{otherwise} \end{cases}\ , \tag{51}$$

and is used as a benchmark set-up for the assessment of the performance of our model in predicting the mixing of droplets from the rich region to the lean region as shown in Figure 12. The rich region is shown as the red coloured sample droplets along the centreline of this figure, while the lean region is shown as the grey coloured sample droplets in the same figure. The initially segregated droplets are expected to mix due to the effect of the turbulent flow field. Two sets of sample droplets were allowed to disperse. The first set of $N_d^{\mathrm{DNS}}$ sample droplets is allowed to disperse along the trajectories $x_d^{\mathrm{DNS}}$, inferred from exact DNS solution $\mathbf{U}(\mathbf{x}, t)$ for the turbulent flow field. The second set of $N_d^{\mathrm{LES}}$ sample droplets, is initialised in the same way as the first one. It is allowed to disperse on the filtered turbulent flow field $\overline{\mathbf{U}}(\mathbf{x}, t)$ resulting in a different set of trajectories $x_d^{\mathrm{LES}}$.

Three simulations with Stokes numbers St = 0.01, St = 0.1 and St = 1.0 were carried out. The input parameters are shown in Table 2. Two levels of resolution ($\Delta = \frac{2\pi}{4}$ and $\Delta = \frac{2\pi}{8}$), using $N_{\mathrm{LES}} = 4$ and $N_{\mathrm{LES}} = 8$ averaging volumes, were used: the coarse mesh with $\mathcal{L}/\Delta = 0.66$, where $\mathcal{L}/\Delta$ is the ratio of the integral scale to the filter width, and the fine mesh with $\mathcal{L}/\Delta = 1.31$.

### *5.3. Results: An analogy between Brownian motion and turbulent diffusion*

In Figure 13 we present the temporal evolution of the ensemble averaged squared displacement for DNS droplets $\left\langle |x_d^{\mathrm{DNS}}(t) - x_d^{\mathrm{DNS}}(t=0)|^2 \right\rangle$ and the displacement $\left\langle |x_d^{\mathrm{LES}}(t) - x_d^{\mathrm{LES}}(t=0)|^2 \right\rangle$ of the droplets dispersing on the filtered

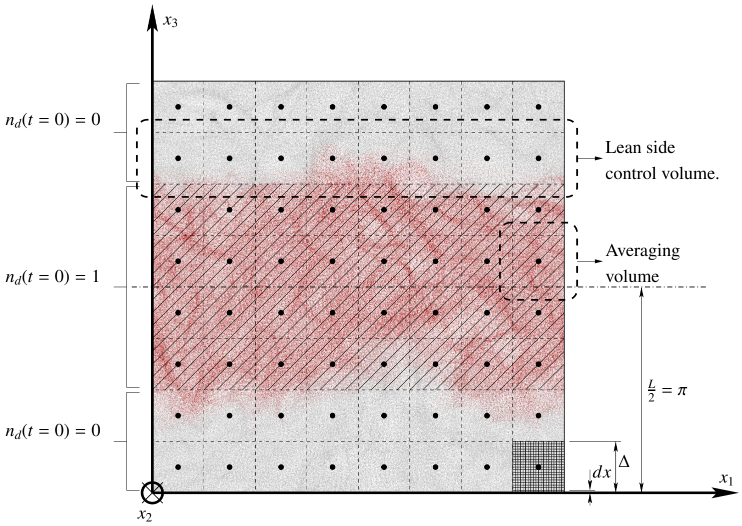

Figure 12: Topology of the numerical experiment. Red dots: sample droplets with $n_d(t=0)=1$. Grey dots: sample droplets with $n_d(t=0)=0$. An example of the DNS mesh is shown in the bottom right corner. The $x_2$ axis is directed into the page as indicated in the bottom left corner of the figure.

| Stokes number<br>St $= \tau_p/\tau_0$ | St = 0.01 | St = 0.1 | St = 1.0 |
|---|---|---|---|
| Kolmogorov scale Stokes number<br>St $= \tau_p/\tau_\eta$ | $\mathrm{St}_\eta = 0.467$ | $\mathrm{St}_\eta = 4.67$ | $\mathrm{St}_\eta = 46.7$ |
| Equilibrium characteristic velocity ratio<br>$\lambda_{inf} = e^{\frac{1}{2}\left(-B\frac{\tau_d}{\tau_t}\right)}$ | 0.997 | 0.975 | 0.778 |

Table 2: Dispersed phase parameters.

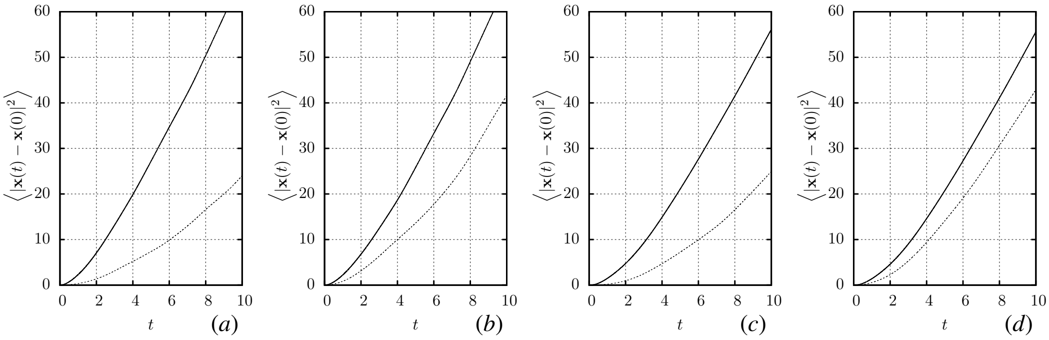

Figure 13: Time evolution of the ensemble averaged squared displacement for droplets dispersing in homogeneous and isotropic turbulence. (*a*) St = 0.1, $\Delta = \pi/2$, (*b*) St = 0.1, $\Delta = \pi/4$, (*c*) St = 1.0, $\Delta = \pi/2$, (*d*) St = 1.0, $\Delta = \pi/4$. Solid curves (——): displacements $\left\langle |x_d^{\mathrm{DNS}}(t) - x_d^{\mathrm{DNS}}(0)|^2 \right\rangle$ of the droplets dispersing in the flow field predicted by the exact DNS solution. Dashed curves (- - -): displacements $\left\langle |x_d^{\mathrm{LES}}(t) - x_d^{\mathrm{LES}}(t = 0)|^2 \right\rangle$ of the droplets dispersing in the flow field predicted by the filtered DNS solution.

DNS field. The ensemble averaging operator is defined as the average value of the Lagrangian variable for $N_d$ Lagrangian droplets within the whole volume of the computational domain $V$. In the general case, for $N_d^{\Omega}$ droplets contained in an arbitrary volume $\Omega$ the ensemble average is defined as:

$$\langle \cdot \rangle^{\Omega} = \frac{1}{N_d^{\Omega}} \sum_{i=1}^{N_d^{\Omega}} (\cdot) \, . \tag{52}$$

The droplets dispersing on the exact turbulent field are expected to mix more intensively compared with those dispersing on the filtered field (46).

The temporal evolution of the squared averaged displacement, shown in Figure 13, refers to the ballistic regime $\sim t^2$ for the initial stage and $\sim t$ (linear diffusive regime) for longer times. The plots presented in Figure 13 highlight similarity between the mixing of the droplets and the characteristic behaviour of the Brownian motion. This supports our approach to the modelling of the subgrid turbulent dispersion as turbulent diffusion (in the same way as the modelling of molecular diffusion), by introducing $D_T = \langle v_i^2 \rangle T_l = \sqrt{\langle v_i^2 \rangle} \mathcal{L}$ (see Xia et al. (92)), where $T_l$ is the Lagrangian integral time scale obtained by the integration of the Lagrangian autocorrelation of the carrier phase velocity. The relation of the droplet diffusion coefficient to the integral time scale justifies the use of the integral scale for the modelling of the diffusion coefficient in (23). As follows from Xia et al. (92), the squared average displacement for the ballistic regime is proportional to $\left\langle v_i^2 \right\rangle t^2$ while for the linear diffusive regime it is proportional to $\langle v_i^2 \rangle T_l t$.

We appreciate that the turbulent diffusion cannot be considered as a Brownian process at a larger scale (droplet interactions are ignored and the turbulent carrier phase flow has little similarity to molecular motion) (85, 36). However, the analysis by Xia et al. (92) and our findings summarised in Figures 13(a-d) suggest that such an analogy can be drawn. Based on this analogy one can use the Fickian diffusion model for the closure of the turbulent diffusion flux (see Equation (19)). This approach is used in our paper.

As expected for both low and high inertia droplets, the dispersion of droplets is faster for those dispersing on the exact turbulent flow field compared to those dispersing on the filtered flow field. This difference increases as the resolution of the flow field decreases. The difference between the dispersion predicted by the filtered solution and the actual dispersion of droplets in turbulence quantifies the turbulent mixing in droplet laden flows (78). As follows from Figure 13, turbulent diffusivity decreases with increasing Stokes numbers. Furthermore, the turbulent diffusion becomes clearer for poorly resolved flows (diagrams (a) and (c)) where the deviation between the inclinations of the curves corresponding to the DNS and the LES droplets is significantly larger than the one shown in diagrams (b) and (d).

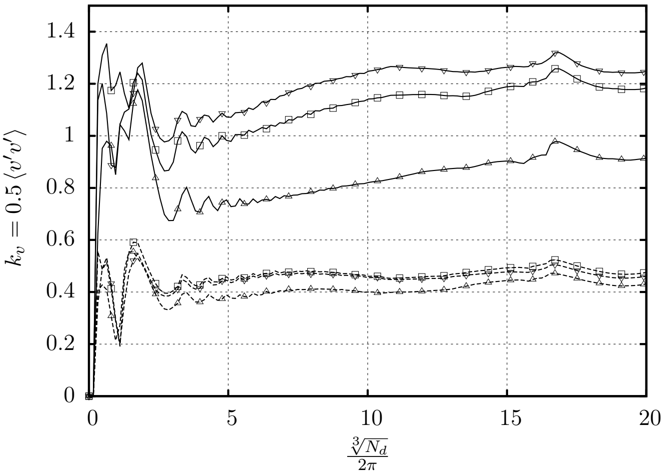

Figure 14: Turbulent kinetic energy of the dispersed phase as a function of the linear number density of droplets. Solid curves (——): droplets dispersing on the turbulent flow field predicted by the exact DNS solution (DNS flow field). Dashed curves (- - -): droplets dispersing on the filtered DNS flow field. Symbols: ▽, St = 0.01; □, St = 0.1; △, St = 1.0

.

### 5.4. *Results: The effect of filtering of the carrier phase on the complexity of the dispersed phase structure*

The turbulent fluctuations of the carrier phase are characterised by a range of scales down to the Kolmogorov microscale $\eta$. It is well known that filtering reduces the span of the turbulent length scales of the flow to the filter cut-off length scale $\Delta$. However, our understanding of how the filtering of the fine features of the carrier phase field affects the motion of the dispersed phase is very limited. The motion of droplets in turbulence demonstrates a spatially correlated structure alongside a random component described as Random Uncorrelated Motion (RUM) (see Meneguz and Reeks (51)). Note that we cannot define Eulerian minimal length scales for the spatial variations of the dispersed phase flow field. As a result, we can estimate the characteristic velocity of the dispersed phase from (22), but we do not know the number of droplets needed to capture the resolved kinetic energy of the dispersed phase.

In Figure 14 we show how the total turbulent kinetic energy for a system of $N_d$ uniformly distributed sampling droplets varies, depending on their linear number density $\sqrt[3]{N_d}/2\pi$ in each direction. The cases of droplets dispersing on the exact and filtered flow fields of homogeneous and isotropic turbulence are shown. The results in this figure refer to the cases where the carrier phase flow field is filtered over eight cells per direction, with $\Delta = \frac{\pi}{4}$. As the number of sampling droplets $N_d$ increases, $k_v$ stabilises (for $\sqrt[3]{N_d}/2\pi > 5$) and constant values are eventually reached. After reaching these constant values, the introduction of additional droplets does not affect the value of $k_v$. In this case, we can assume that these sampling droplets are representative for the description of the fluctuations of the dispersed phase, and the dispersed phase is resolved.

For the droplets dispersing on the DNS field (solid curves in Figure 14) $k_v$ increases until it reaches a plateau for $\sqrt[3]{N_d}/2\pi > 10$ (this corresponds to $N_d = 343,000$) for the lower inertia droplets (St $\leq 0.1$). For the high inertia droplets (St = 1.0), this plateau is reached for $\sqrt[3]{N_d}/2\pi > 16$. This means that we need very high numbers of sampling droplets $N_d > 10^6$ to resolve the DNS fields. For the droplets dispersing on the filtered DNS flow field (dashed lines in Figure 14), however, the number of droplets needed for the resolution of the total kinetic energy is greater than four ($\sqrt[3]{N_d}/2\pi > 4$). This corresponds to $N_d = 25^3$ droplets.

This number is comparable to the number of filtering volumes per direction (8 filtering volumes in each direction). This indicates that the filtering of the carrier phase flow field results in a reduction in the resolution needed to capture the resolved scale fluctuations of the carrier phase. The previous implementation of the model (see Papoutsakis et al. (63)) was performed with just one droplet per averaging volume.

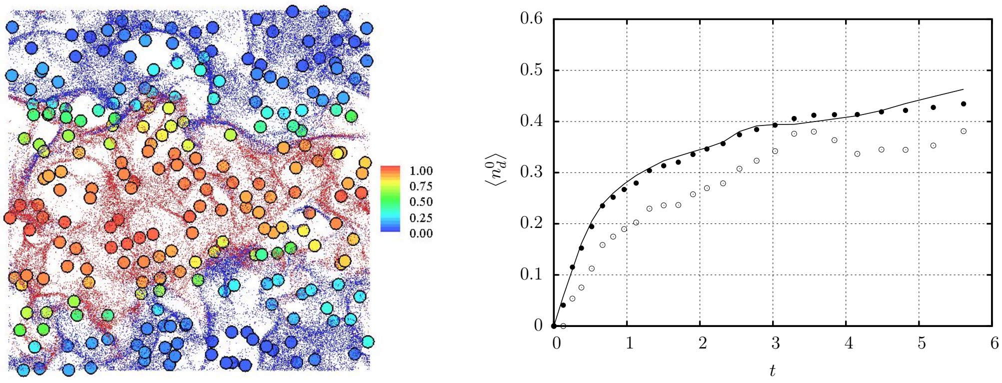

($a$) ($b$)

Figure 15: Model predictions of droplet dispersion by decaying homogeneous and isotropic turbulence. (a) Droplet distribution at $t = 1.0$ for a slice of the domain of width $\pi/16$. Dots show individual droplets dispersed on the DNS flow field. The colour of the dots (blue or red) refers to the droplet number densities $n_d(0)$ (0 or 1) at their initial positions. Filled circles show sampling droplets dispersing on the filtered flow field; their colours refer to zero moments of the number density $n_d^0(t)$ (in the absence of diffusion this moment gives us the initial distribution of the droplet number density (1 or 0); intermediate values of this moment are related to the effect of the diffusion). (b) Mean values of the zero moment of $n_d^0(t)$ in the averaging volumes located at the lean side control volume (see Figure 12) $\left[\left\langle n_d^0 \right\rangle\right]$ ($\langle\cdot\rangle$ indicates averaging in each computational cell, while $[\cdot]$ indicates averaging over the control volume shown in Figure 12, containing $N_{\text{LES}} \times N_{\text{LES}}$ cells). Solid curve (——) refers to DNS results; symbols ○ refer to filtered DNS results without diffusion; symbols ● refer to filtered DNS results with diffusion.

### 5.5. *Results: Modelling turbulent diffusion of droplets in HIT using the FLA model for a droplet cloud in a turbulent flow field*

To describe droplet transport in the homogeneous turbulent flow, both in DNS and LES fields, the Fully Lagrangian Approach (FLA) is used. Having initialised the droplet positions ($x_d^{\text{DNS}}$ and $x_d^{\text{LES}}$), their velocities ($V_i^{\text{DNS}}$ and $V_i^{\text{LES}}$), the elements of the Jacobian matrix $J_{ij}$ and the corresponding rates $\omega_{ij}$, the dispersion of the DNS and LES droplets is integrated over time. In contrast to the original FLA model we also solve the initial value problem for the droplet number density $n_d$ (see 25) and the droplet turbulent kinetic energy $k_v$ (see 22). As follows from Meneguz and Reeks (51), and Ijzermans et al. (39) the absolute value of the determinant of the Jacobi matrix $\|\mathbf{J}\| \equiv |\det J_{ij}|$ in (25) allows us to obtain the moments of the droplet number densities $n_d^a = n_d/\|\mathbf{J}\|^{a-1}$ as in (38). The ensemble averages of the moments of the number densities, defined in the Equation (52), are used:

$$\left\langle n_d^a \right\rangle = \left\langle \frac{n_d}{|\mathbf{J}|^{a-1}} \right\rangle , \tag{53}$$

where the averaging is performed within the LES cell and $n_d$ is defined by (25). When evaluating the droplet number density within an averaging volume we are primarily interested in the total number of droplets contained in this volume, controlled by the zero moment $n_d^0$ of the number density. The results of our calculations for $128^3$ individual droplets with Stokes number $\text{St} = 0.1$ are shown in Figure 15. As follows from this figure, turbulence plays an important role in droplet mixing and should be taken into account when the FLA is applied to turbulent flows.

The zeroth moments of droplet density versus normalised time for various combinations of St and $\Delta$ are shown in Figure 16. As follows from this figure, the difference between the values of $\left\langle n_d^0 \right\rangle$, predicted by the models, taking into account and ignoring the effects of diffusion, is greater for the low resolution cases ($\Delta = \pi/2$) (where the flow integral scale is not fully resolved) than for the high resolution ones ( $\Delta = \pi/4$). The estimated dispersion time for the model without diffusion is about twice as long as the dispersion time predicted by the model taking into account the effect of diffusion.

In all cases under consideration the results predicted for LES droplets with diffusion turned out to be close to the DNS results, except for the cases of the high-inertia droplets shown in diagrams (e) and (f) in Figure 16. In the latter cases the model tends to underestimate the dispersion of the droplets conveyed by the turbulent flow field. This can be attributed to an increase in the turbulence characteristic time $\tau_t$ after the initial stages of droplet mixing, as shown in Table 1. Turbulent diffusion is more sensitive to accurate prediction of turbulent time scales for droplets with larger Stokes numbers than for droplets with smaller Stokes numbers.

### 5.6. *Results: Higher moments of droplet number density in HIT using the FLA model for a droplet cloud in a turbulent flow field*

The higher moments of the droplet number density provide information on the localised compression or dilation of the dispersed phase (see Meneguz and Reeks (51)). In our further analysis we will be primarily interested in the first moment when:

$$\left\langle n_d^1 \right\rangle = \langle n_d \rangle \ , \tag{54}$$

where $n_d$ is defined by Eq. (2.18) without taking into account the effects of diffusion for DNS droplets. As follows from the latter equation, $n_d$ is proportional to $1/J$. The localised peaks in $1/J$, clearly seen in Figure 17(b), show the localised compression zones. These localised peaks in $1/J$ are not obvious for the lower and higher inertia droplets (see Figure 17 (a) and (c)). The same plots as shown in Figure 17(c), for St = 1.0 but for longer time $t = 23.2$, are presented in Figure 17(d). As follows from this figure, the localised compression zones (similar to those seen in Figure 17(b)) can be observed for this Stokes number at longer times. The behaviour of $1/J$ shown in these figures is rather different. In the case shown in Figure 17(a) the values of $1/J$ are well below 10 in the whole domain, while in the case shown in Figure 17(c) broad peaks in $\log(1/J)$ can be clearly seen with $1/J$ reaching and exceeding 10 (the larger values of $1/J$ are truncated to 10 for illustrative purposes).

The time evolution of the zeroth and first moments of the droplet number density in the control volume shown in Figure 12 for St = 0.01 is shown in Figures 18 and 19(a,b). As one can see from these figures, both zeroth and first moments predicted by all models increase with time. In all LES cases shown in these figures, the Jacobian is very close to unity. Hence, the predicted values of the zeroth and first moments are expected to be very close. This is exactly what can be seen in the above mentioned figures. As in the cases shown in Figure 16, the zeroth moments for LES droplets, taking into account diffusion, are reasonably close to the zeroth moments of DNS droplets. At the same time, the first moment for LES droplets, taking into account diffusion, is much less than the first moment of DNS droplets. This is attributed to the fact that the filtering of the carrier phase flow field causes the smoothing of the droplet trajectories. This is expected to mitigate the dilation/compression caused by diverging/converging trajectories. Note that there are no spikes in the temporal evolution of the first moment of the droplet number density in the plots shown in Figure 19(a,b). These spikes might have been indications of droplet trajectory intersections.

For Stokes number St = 0.1 (intermediate inertia) the effect of trajectory intersections (indicated by the spikes in the first moment) can be clearly seen in Figure 17(c,d). This is consistent with the results shown in Figure 17(b). These trajectory intersections cannot be seen for the droplets dispersing on the filtered flow field. Although trajectory intersections can be clearly seen for the droplets dispersing on the exact DNS solution, the droplets dispersing on the filtered flow field do not show the same behaviour.

Results similar to those shown in Figures 16 and 19, but for 8 times more droplets, are presented and discussed in Appendix A. As follows from the analysis presented in this appendix, the values of the first and second moments of the droplet number densities are practically unaffected by the number of sampling droplets.

In Figure 20 we presented the time evolution of the compressibility $\langle \ln(|\mathbf{J}|) \rangle$ for 3 Stokes numbers converging to the long term net compressibility. Compressibility, as introduced by Ijzermans et al. (39), is related to the average compressibility of the dispersed phase $\langle \nabla \mathbf{V_d} \rangle$, but only in the case that the velocity field of the dispersed phase is single valued and continuous. As shown by Meneguz and Reeks (51), for a turbulent flow field the sign of the compressibility indicates the topological distribution of compression and dilation regions. The compressibility tends towards positive and negative values for large and small Stokes numbers, respectively. The deviation of compressibility rate from zero implies that the concentration field is not in an equilibrium state. As follows from Figure 20, for low Stokes numbers (St = 0.01) this compressibility is close to zero for all times, which implies that the Jacobian is close to unity. For the intermediate and high Stokes numbers (St = 0.1 and St = 1) the time evolution of the compressibility becomes complex, but in both cases it tends towards constant values in the long time limit.

We have identified two types of response for the droplets in a turbulent field. The first one is the mixing of the droplets and the second one is their segregation leading to trajectory intersections. The effect of filtering of the carrier phase flow field in the LES framework is different for each one of these mechanisms.

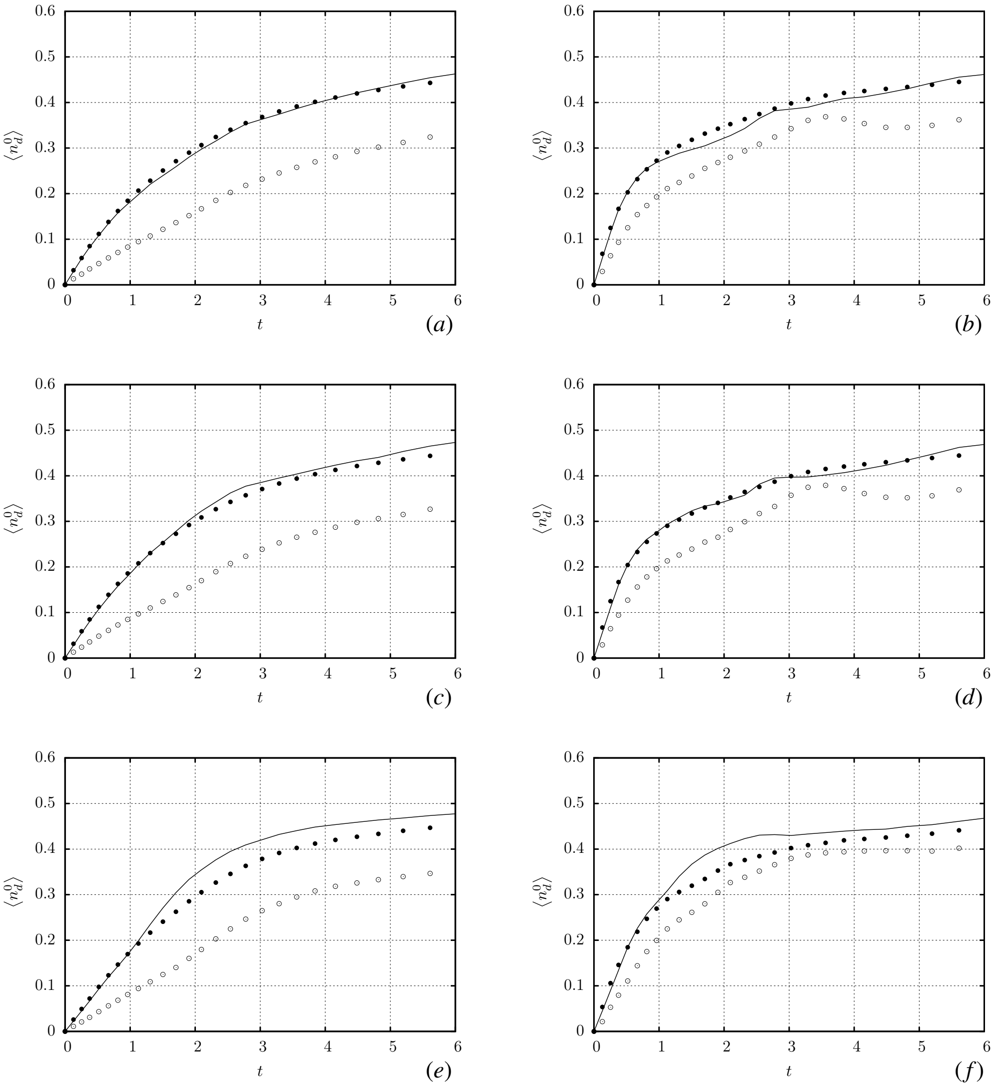

Figure 16: Average values of the zero moment of droplet number densities in the lean side control volume $\left[\left\langle n_d^0 \right\rangle\right]$ (see Figures 12 and 15). Simulations were carried out for the same numbers ($64^3$) of LES and DNS droplets. (*a*) St = 0.01, $\Delta = \pi/2$, (*b*) St = 0.01, $\Delta = \pi/4$, (*c*) St = 0.1, $\Delta = \pi/2$, (*d*) St = 0.1, $\Delta = \pi/4$, (*e*) St = 1.0, $\Delta = \pi/2$, (*f*) St = 1.0, $\Delta = \pi/4$. Solid curves (——) refer to DNS droplets. Symbols ○ refer to LES droplets without diffusion, symbols ● refer to LES droplets with diffusion.

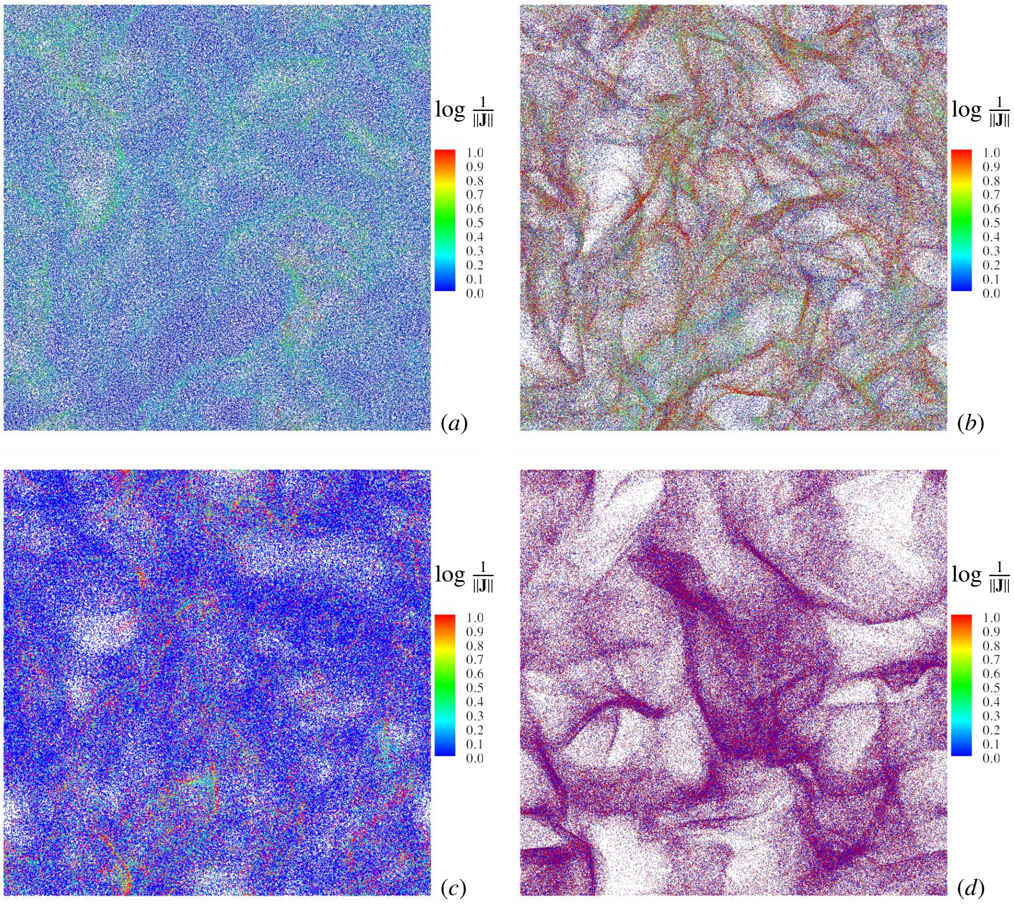

Figure 17: Droplet distributions $x_d^{\mathrm{DNS}}$ for 3 Stokes numbers (*(a)* St = 0.01, *(b)* St = 0.1, *(c)* St = 1.0) at $t$ = 1.0 and (*(d)* St = 1.0) at $t$ = 23.2. The colour of each droplet indicates the logarithm of the magnitude of the inverse of the Jacobian.

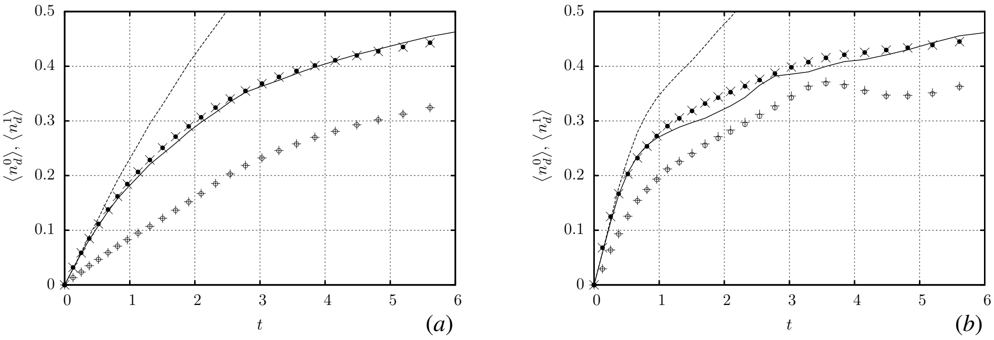

Figure 18: Average values of the zeroth and first moments of the number density in the control volume shown in Figure 12. Simulations were carried out for $64^3$ LES and DNS droplets. (*a*) St = 0.01, $\Delta = \pi/2$, (*b*) St = 0.01, $\Delta = \pi/4$. Solid curves (——) refer to zeroth moments of DNS droplets. Dashed curves (– – –) refer to first moments of DNS droplets. Symbols: ○ refers to $\left\langle n_d^0 \right\rangle$ for LES droplets without diffusion, ● refers to $\left\langle n_d^0 \right\rangle$ for LES droplets with diffusion, + refers to $\left\langle n_d^1 \right\rangle$ for LES droplets without diffusion, × refers to $\left\langle n_d^1 \right\rangle$ for LES droplets with diffusion.

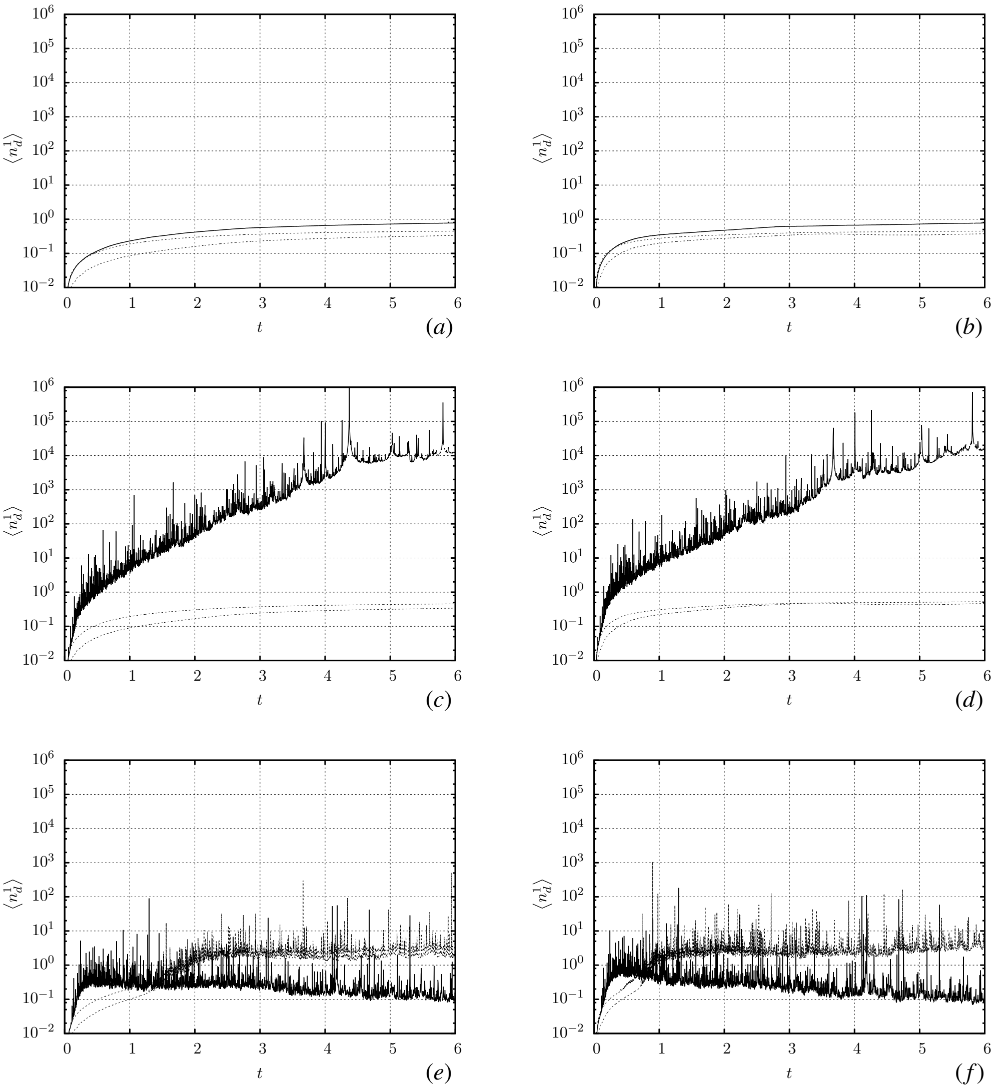

Figure 19: Average values of the first moments of the number density in the control volume shown in Figure 12 ($\left[\left\langle n_d^1 \right\rangle\right]$). Simulations were carried out for $64^3$ LES and DNS droplets. ($a$) St = 0.01, $\Delta = \pi/2$, ($b$) St = 0.01, $\Delta = \pi/4$, ($c$) St = 0.1, $\Delta = \pi/2$, ($d$) St = 0.1, $\Delta = \pi/4$, ($e$) St = 1.0, $\Delta = \pi/2$, ($f$) St = 1.0, $\Delta = \pi/4$. Solid curves (——) refer to DNS droplets. Upper dashed curves (- - -) refer to LES droplets with diffusion. Lower dashed curves (- - -) refer to LES droplets without diffusion.

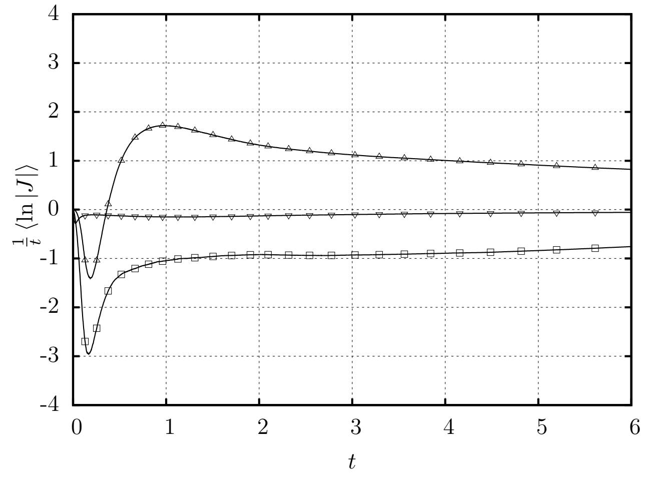

Figure 20: Time evolution of $\langle \ln(|\mathbf{J}|)/t \rangle$ (long term net compressibility). Symbols: ▽ St = 0.01, □ St = 0.1, △ St = 1.0.

Increasing Stokes numbers result in reduced droplet mixing. This is confirmed by the measurements of the averaged displacement of the droplets (78) on the filtered field, shown in Figure 13, where the deviation between the LES and the DNS result reduces for large Stokes numbers.

Droplet trajectory crossing is affected by the small scales, as shown in Figure 19. In this figure we observe that the small scales are responsible for the droplet intersections for St=0.1 and expedite the onset of the intersections for St= 1.0. At the same time, the large scales do not induce intersections for St= 0.1 but begin to affect trajectory intersections at St= 1.0. We attribute this behaviour to the Stokes number defined at each length scale. The droplet-flow interaction for the large turbulent scales of the flow is characterised by small Stokes numbers, whereas the small turbulent scales of the flow interact with droplets in a high inertia ballistic regime which is characterised by large Stokes numbers. As a result, an increase in the macroscopic Stokes number leads to a situation where the large scales start to affect droplet trajectory intersections. For the small scales, the Stokes number can increase further, to a point where the small scales do not affect either the intersection of the droplets or their segregation (20, 21). In (21), the limit where the subgrid fluctuations do not affect particle segregation is set at St> 5.

The differences in the temporal evolution of the first moments of the droplet number density, predicted by DNS and LES shown in the Figure 19, support the need to develop a second order model for the local first moment of the droplet number density distribution. The calculations of zeroth moments of the droplet number density account for the mass exchange due to the unresolved turbulent mixing of the droplets. Investigations based on the second order model, as presented in Section 4, could provide information for the unresolved dilation and compression shown in Figure 19, and enhance our understanding of the evolution of net compressibility for the dispersion of inertia particles in turbulent flows.

## 6. Discussion

To summarise our results, we have generalised the previously developed FLA to enable us to apply it to the modelling of droplet clouds in turbulent flows. The FLA equations for the conservation of mass and momentum were derived for an elementary Lagrangian volume in an unresolved filtered flow field. The unresolved pressure arising in the FLA momentum equation is assumed to be negligible. This assumption is supported by direct simulations of a large number of droplets undulating in an oscillating one-dimensional carrier phase flow (Knudts tube). The unresolved turbulent diffusion flux was modelled based on the Fickian diffusion assumption, using the similarities of the subgrid droplet motion and the Brownian motion drawn from direct simulations of the homogeneous isotropic turbulence (HIT). The derivation of a second order extension of the FLA was presented. The latter overcomes the problem of infinite number densities in the standard FLA in the vicinity of caustic formations, and most importantly, defines the length scale, necessary for the implementation of the FLA in the LES framework. The capabilities of the FLA in identifying the fine structures of the dispersed phase formations were presented. We also presented an integrated platform for the modelling of dispersed flows in the LES context using the FLA.

The FLA incorporates the Eulerian conservation equation for the droplet number density in the Lagrangian description of the droplets dispersed by the carrier phase flow field. It describes the dispersed phase as a continuum in the same manner as the standard Eulerian approach. We assumed that a dilute system of discrete droplets can be considered as a pressureless continuum, which is consistent with the assumptions of the dusty gas model used by many authors, including Marble (45) and Crowe et al. (17). The consideration of a system of discrete droplets (dispersed phase) in multiphase flows as a continuum with exact instantaneous field equations for the particle phase parameters has a very long history, beginning in the early 1950s (e.g. mathematical theory of aerosols by Fuchs (26) and Robinson (72)) and continuing into the 1960s (e.g. two-fluid dusty-gas model by Carrier (7), Saffman (75), Marble (45), Soo (83), and Rudinger (74)). The continuum description of discrete particles was endorsed in a series of approaches to turbulence modelling in dispersed flows (see (85)). In (54), a rigorous mathematical justification of the continuum description for discrete particles is presented.

The modelling choice of representing the dispersed phase using exact instantaneous fields is further supported by recent modelling approaches for turbulent dispersed flows (24, 71, 60, 78). In (24) this assumption is based on the investigation of the dispersed phase spatial correlation. Modern modelling approaches for turbulent dispersed flows incorporate correlated and quasi-Brownian components (1, 23), used in the two-fluid models suggested in (71, 60). In the Approximate Deconvolution Method (ADM) (78, 79, 47) a field description is used for the dispersed phase by introducing an approximate de-convoluted field (46).

Our generalised FLA introduces a dual representation of the dispersed medium. At the first level, even for the case of the classical FLA for laminar flows, FLA is derived starting from the integral particle mass balance equation. At this level, the introduction of the Jacobian accounts for the crossing of the trajectories, and the folding of the dispersed continuum. For a Lagrangian moving cloud, FLA tackles the problem of multivalued velocity fields, allowing multiple overlapping of the particulate continuum in cases of trajectory crossings. This feature of the FLA is illustrated in Figure 11, where two types of unmixing can be seen at the trajectory of the reference particle. The first is related to the crossing of the reference particle trajectory with other trajectories, where a multivalued dispersed flow field is represented successfully by the FLA. The second is related to compression of the trajectories of the cloud itself. Our findings, summarised in Figure 19, show the smoothing of the trajectory intersections by the filtering of the carrier phase flow field (cf. (20, 21, 46)). This supports our modelling decision to represent the dispersed phase as a folded single valued continuum.

We presented a novel second order extension of the FLA which allows us to calculate the determinant of second-order derivatives of the Eulerian coordinates with respect to Lagrangian ones (Hessian) for the deformed particulate continuum. The suggested method overcomes the problem of infinite number densities of the standard FLA in the vicinity of caustic formations. The interpretation of singularities in the number density field, which arise from the standard FLA approach has been a very delicate issue (cf. Fessler et al. (22), Reeks (70), Meneguz and Reeks (51), Ijzermans et al. (39)). This requires care in the calculation of spatial averages of the number density Ijzermans et al. (39). The second order FLA provides a robust new tool for the calculation of the number density in the presence of caustic formations. This tool allows us to predict the occurrence of the caustic and the value of the number density on that caustic.

State of the art approaches to the modelling of dispersed flows (52, 28) allow one to take into account complex interactions between the dispersed and the carrier phase in the LES context. The effect of turbulence in the formulation of our generalised FLA is expressed in terms of the unclosed turbulent diffusion flux and the subgrid pressure. When we applied our method to calculation of the turbulent diffusion, we used a standard Fickian diffusion approach based on the similarities of the subgrid droplet motion to Brownian motion (Xia et al. (92) and Fung et al. (27)). This modelling choice was further investigated by means of direct simulations of Homogeneous Isotropic Turbulence (HIT). Furthermore, the unresolved pressure term was ignored, based on well documented assumptions (2), assessed in Section 3.

In (20), the analysis of the effect of the subgrid scales on droplet diffusivity and segregation (which can result in compression and dilatation for low Stokes numbers, and to trajectory intersections and RUM for high Stokes numbers (49)) led to the conclusion that for intermediate Stokes numbers St$<0.5$ the Lagrangian models are not well suited, although the particles are characterised by significant inertia. The Eulerian closure of the droplet diffusivity aims to address this issue. Cernick et al. (8) presented a detailed comparison of the Approximate Deconvolution Method (ADM) (78, 79) and the stochastic modelling approach presented in Berrouk et al. (4) for inertial particles and trajectory intersections, highlighting the modelling challenges and their shortcomings in terms of capturing the effect of trajectory intersections. The novelty of the FLA is that the compression and dilatation of the dispersed phase are accounted for by the integration of the Jacobian and the Hessian matrices using a single particle. The initial value problem for $J$ and $H$ is the expression of the history of the cloud along its trajectory. Our aim is to deliver an integrated platform for the FLA that takes into account the effect of unresolved turbulent fluctuations in terms of the diffusion flux and the pressure term and, most importantly, that provides a link between the method and an appropriate length scale (cf. Section 4).

## 7. Conclusion

A combined Eulerian-Lagrangian approach to effective and low-cost numerical modelling of mixing and un-mixing of inertial droplets in turbulent gas-droplet flows is proposed. The results of simulations for a statistically significant number of individual droplets that disperse in a carrier phase, described by DNS of decaying homogeneous and isotropic turbulence, are compared with the results obtained from the application of the suggested model using the filtered DNS solution in the LES framework.

The parameters of the particulate medium (including the particle number density) are calculated using the Fully Lagrangian Approach along the chosen droplet trajectories. The contribution of subgrid velocity fluctuations observed as mixing of the dispersed phase can be modelled by an additional particle mass flux described by a Fickian diffusion law with a scalar diffusion coefficient. This was supported by investigating the mixing of droplets in DNS of homogeneous and isotropic turbulence and identifying characteristics similar to those of Brownian motion.

The droplet dispersion model is based on the assumption that the unresolved momentum flux is small in comparison with the unresolved mass flux, the validity of which is demonstrated for a simple one-dimensional flow in a Knudt tube. In this analysis it has also been shown that the droplets undulate due to the effect of harmonic oscillations and un-mix, creating structures that follow the integral scale of the flow. It was observed that droplet mixing and un-mixing take place at the same time, as in the DNS simulations of homogeneous and isotropic turbulence.

Both in the one-dimensional model and the 3D DNS simulations, droplets disperse due to flow fluctuations. Also, they form agglomeration patterns (caustics) due to these fluctuations. This agglomerated distribution of droplets expands in a classical Brownian fashion.

It is shown that un-mixing of droplets leads to the creation of compression regions on the integral length scale of turbulent flow. This un-mixing takes place simultaneously with the turbulent diffusion. The un-mixing is quantified by the first moment of the droplet number density. The value of this moment is controlled by the determinant of the Jacobi matrix of transition from Eulerian to Lagrangian coordinates. The evolution of the first moment of the number density is visibly affected by the filtering of the turbulent field. This results in unresolved un-mixing of the dispersed phase in the filtered carrier phase field.

The second order extension of the FLA, showing the spatial structure of the number density field, is presented. This analysis allows us to describe how the FLA approach can model the detailed structure of caustic formations.

## Acknowledgments

The authors are grateful to the EPSRC, UK (grants EP/K005758/1, EP/M002608/1 and EP/R012024/1), Royal Society (UK) (grant IE 160014) and the Russian Foundation for Basic Research (grants No. 17-01-00057 and 16-51-10024) for their financial support.

## Appendix A. The formulation of the initial value problem for the Hessian

We present a method of calculating the Hessian $H = \frac{\partial^2 x}{\partial x_0^2}$ of the transformation from the Lagrangian to the Eulerian coordinates of the dispersed continuum. In the classical FLA, the Jacobian $J$ is calculated by introducing the auxiliary variable $\omega$ which is the time derivative of the Jacobian:

$$\omega = \frac{\partial J}{\partial t} = \frac{\partial}{\partial t}\left(\frac{\partial x}{\partial x_0}\right) = \frac{\partial V}{\partial x_0} \, . \tag{A.1}$$

In the general case where $\frac{\partial V}{\partial t} = f(S)$, $S = U - V$, $\omega$ is obtained by solving the following initial value problem:

$$\frac{\partial \omega}{\partial t} = \frac{\partial}{\partial t}\left(\frac{\partial V}{\partial x_0}\right) = \frac{\partial}{\partial x_0}\left(\frac{\partial V}{\partial t}\right) = \frac{\partial}{\partial x_0}\left(f(S)\right) = \frac{\partial f(S)}{\partial S}\left(\frac{\partial S}{\partial x_0}\right) = \frac{\partial f(S)}{\partial S}\left(\frac{\partial U}{\partial x}\frac{\partial x}{\partial x_0} - \omega\right) . \tag{A.2}$$

For a Stokes force $f(S) = S/\tau_d$ acting on the droplet, the expression for $\omega$ becomes:

$$\frac{\partial \omega}{\partial t} = \frac{1}{\tau_d}\left(\frac{\partial U}{\partial x}\frac{\partial x}{\partial x_0} - \omega\right) = \frac{1}{\tau_d}\left(\frac{\partial U}{\partial x}J - \omega\right) , \tag{A.3}$$

where Equation A.2 is integrated using the initial condition $\omega = \frac{\partial V}{\partial x}\big|_{t=0}$ stemming from Equation A.1. For the derivation of an expression of the Hessian $H$, we follow an approach similar to the one used for the calculation of the Jacobian. This is done by introducing the auxiliary variable $\psi$ which is defined as the time derivative of the Hessian, as follows:

$$\psi = \frac{\partial H}{\partial t} = \frac{\partial}{\partial t}\left(\frac{\partial}{\partial x_0}\left(\frac{\partial x}{\partial x_0}\right)\right) = \frac{\partial}{\partial x_0}\left(\frac{\partial}{\partial t}\left(\frac{\partial x}{\partial x_0}\right)\right) = \frac{\partial^2 V}{\partial x_0^2} \, . \tag{A.4}$$

The time derivative of $\psi$ can be presented as:

$$\frac{\partial \psi}{\partial t} = \frac{\partial}{\partial t}\left(\frac{\partial^2 V}{\partial x_0^2}\right) = \frac{\partial^2}{\partial x_0^2}\left(\frac{\partial V}{\partial t}\right) = \frac{1}{\tau_d}\frac{\partial^2}{\partial x_0^2}(U - V) = \frac{1}{\tau_d}\left(\frac{\partial^2 U}{\partial x_0^2} - \frac{\partial^2 V}{\partial x_0^2}\right) = \frac{1}{\tau_d}\left(\frac{\partial^2 U}{\partial x_0^2} - \psi\right) , \tag{A.5}$$

where the droplet acceleration $\frac{\partial V}{\partial t}$ is modelled using the Stokes approximation. The derivative $\frac{\partial^2 U}{\partial x_0^2}$ can be estimated as:

$$\frac{\partial^2 U}{\partial x_0^2} = \frac{\partial}{\partial x_0}\left(\frac{\partial U}{\partial x_0}\right) = \frac{\partial}{\partial x_0}\left(\frac{\partial U}{\partial x}\frac{\partial x}{\partial x_0}\right) = \frac{\partial}{\partial x_0}\left(\frac{\partial U}{\partial x}\right)\frac{\partial x}{\partial x_0} + \frac{\partial U}{\partial x}\frac{\partial}{\partial x_0}\left(\frac{\partial x}{\partial x_0}\right) = \frac{\partial}{\partial x_0}\left(\frac{\partial U}{\partial x}\right)J + \frac{\partial U}{\partial x}H \, . \tag{A.6}$$

Taking into account that:

$$\frac{\partial}{\partial x_0}\left(\frac{\partial U}{\partial x}\right) = \frac{\partial}{\partial x}\left(\frac{\partial U}{\partial x}\right)\frac{\partial x}{\partial x_0} = \frac{\partial^2 U}{\partial x^2}J \tag{A.7}$$

the derivative $\frac{\partial^2 U}{\partial x_0^2}$ is calculated as:

$$\frac{\partial^2 U}{\partial x_0^2} = \frac{\partial}{\partial x_0}\left(\frac{\partial U}{\partial x}\right)\frac{\partial x}{\partial x_0} + \frac{\partial U}{\partial x}\frac{\partial}{\partial x_0}\left(\frac{\partial x}{\partial x_0}\right) = \frac{\partial^2 U}{\partial x^2}JJ + \frac{\partial U}{\partial x}H \, . \tag{A.8}$$

Finally the time derivative of $\psi$ can be presented as:

$$\frac{\partial \psi}{\partial t} = \frac{1}{\tau_d}\left(\frac{\partial^2 U}{\partial x^2}J^2 + \frac{\partial U}{\partial x}H - \psi\right) . \tag{A.9}$$

The above result could be obtained by taking the derivative over $x_0$ of the expression for $\omega$ in Equation A.2. The initial conditions for the initial value problem A.9 are inferred from Equation A.4. For $t = 0$ the Lagrangian derivative coincides with the Eulerian derivative. The initial value for $\psi(t = 0)$ is the following:

$$\psi(t = 0) = \frac{\partial^2 V}{\partial x^2} \, . \tag{A.10}$$

Assuming that at the initial time instant the dispersed continuum is not deformed, $H(t = 0) = 0$ is used as the initial value for $H$.

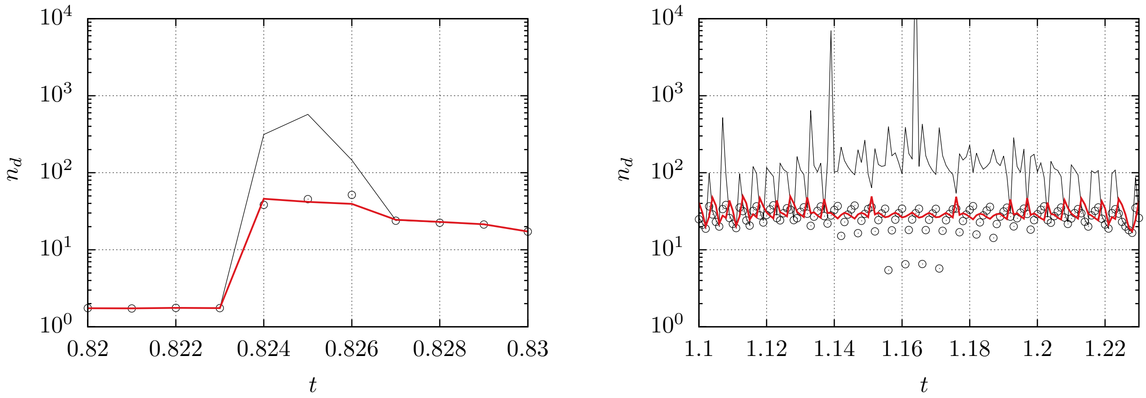

Figure A.1: **Left:** Total number density $\hat{n}_d$ along the $x_0 = -0.25$ droplet trajectory assuming an averaging volume with $2R_\epsilon = 0.001$, focusing on the time interval close to the occurrence of the first number density peak. Solid red curve: result inferred from the second order FLA. Circles: result inferred from box counting on the same length scale. Thin curve: result inferred from the standard FLA. **Right:** Total number density $\hat{n}_d$ along the $x_0 = -0.25$ droplet trajectory assuming an averaging volume with $2R_\epsilon = 0.001$, focusing on the time interval close to the occurrence of the second number density peak. Solid red curve: result inferred from the second order FLA. Circles: result inferred from box counting on the same length scale. Thin curve: result inferred from the standard FLA.

## Appendix B. The results from the box counting versus the results inferred from the standard FLA and the second order FLA

In Figures A.1 we present the total number density along the $x_0 = -0.25$ droplet trajectory focusing on the time instances of the first and the second peaks of the droplet number density (see Section 4). As can be seen from this figure, the second order FLA predicts number densities close to those inferred from the box counting calculations. As the reference particle crosses different filtering volumes (boxes), oscillations in the number density, predicted by the second order FLA, are observed. Even larger oscillations are observed in the box counting result. The results predicted by standard FLA are substantially affected by the singularities in the calculated field. Note that the box counting method still does not provide a converged result even if $10^6$ droplets are used in calculations.

## Appendix C. Investigation of the independence of the results for the turbulent mixing model to the total number of FLA droplets

In Figure A.2 results similar to those presented in Figure 16 but for $N_d^{\text{LES}} = 128^3$ LES and DNS sampling droplets are shown. Although 8 times more sampling droplets were used in the simulations, the results of which are shown in Figure A.2, than in the simulation the results of which are shown in Figure 16, there were no significant differences in the final results. Note that to obtain the results shown in Figure 15(b) we used only $N_d^{\text{LES}} = 16^3$ LES sampling droplets for the modelling of $N_d^{\text{DNS}} = 128^3$ sampling droplets for the same conditions as in Figures 16(d) and A.2(d).

As we can see from Figures 15(b), 16(d) and A.2(d), the number of sampling droplets used for the modelling of the dispersed phase does not affect the results as long as the energy of the fluctuations of the dispersed phase has been adequately resolved (cf. the discussion of Figure 14). Also, increasing the number of LES sampling droplets does not improve the LES results without diffusion.

In Figure A.3 results similar to those presented in Figure 19, but for $N_d^{\text{LES}} = 128^3$ LES and DNS sampling droplets, are shown. As in the case of Figures A.2 and 16, the results shown in Figures A.3 and 19 are rather similar. This implies that the turbulent diffusion of the dispersed phase is controlled by the filtering of the carrier phase flow field and not by the number of sampling droplets.

[1] Alipchenkov, V., Zaichik, L., Oct 2008. Subgrid continuum modeling of particle motion in a turbulent flow. Fluid Dynamics 43 (5), 731–744. URL `https://doi.org/10.1134/S0015462808050074`

[2] Armenio, V., Piomelli, U., Fiorotto, V., 1999. Effect of the subgrid scales on particle motion. Physics of Fluids 11 (10), 3030–3042. URL `https://doi.org/10.1063/1.870162`

[3] Berlyand, M., 1974. Air Pollution and Atmospheric Diffusion. Halsted Press.

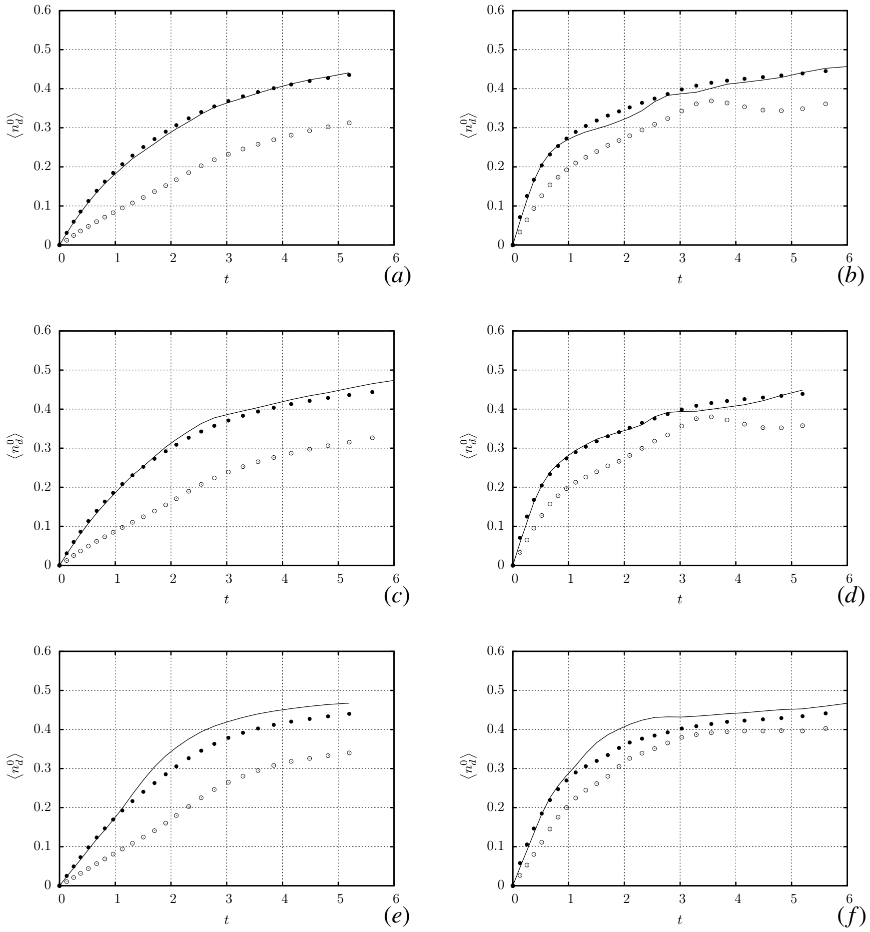

Figure A.2: The same as Figure 16 but for $128^3$ LES and DNS sampling droplets. (*a*) St = 0.01, $\Delta = \pi/2$, (*b*) St = 0.01, $\Delta = \pi/4$, (*c*) St = 0.1, $\Delta = \pi/2$, (*d*) St = 0.1, $\Delta = \pi/4$, (*e*) St = 1.0, $\Delta = \pi/2$, (*f*) St = 1.0, $\Delta = \pi/4$. Solid curves (——) refer to DNS droplets. Symbols ○ refer to LES droplets without diffusion, symbols ● refer to LES droplets with diffusion.

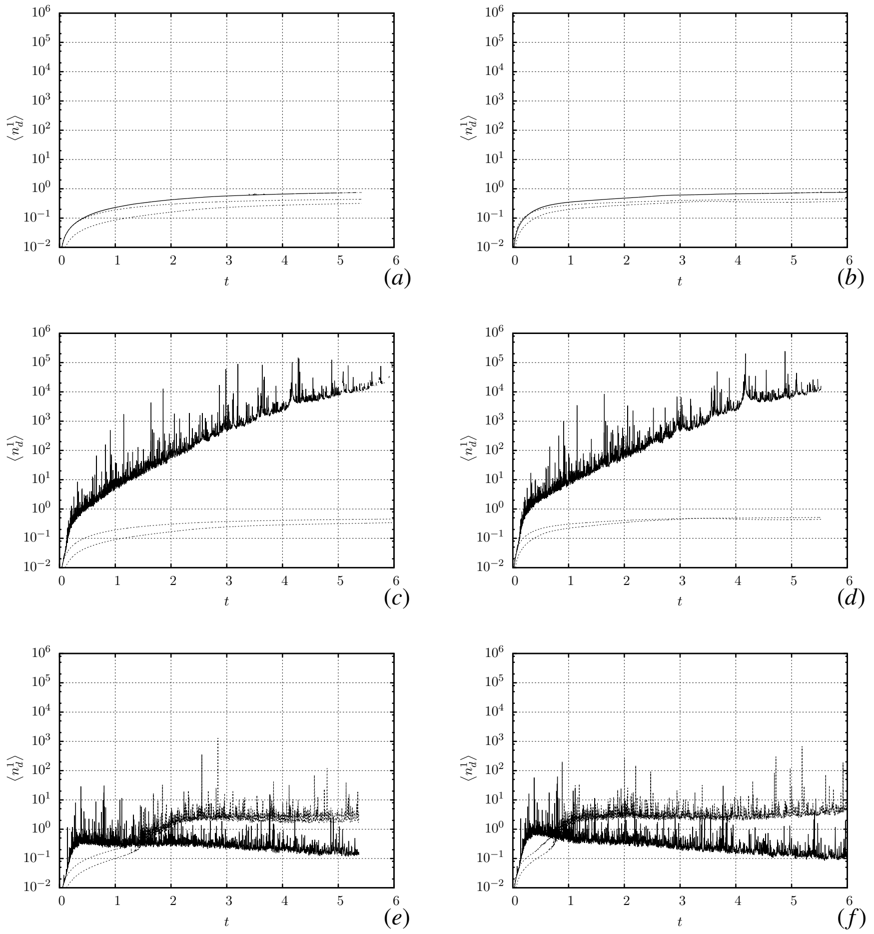

Figure A.3: The same as Figure 19 but for $128^3$ LES and DNS sampling droplets. (*a*) St = 0.01, $\Delta = \pi/2$, (*b*) St = 0.01, $\Delta = \pi/4$, (*c*) St = 0.1, $\Delta = \pi/2$, (*d*) St = 0.1, $\Delta = \pi/4$, (*e*) St = 1.0, $\Delta = \pi/2$, (*f*) St = 1.0, $\Delta = \pi/4$. Solid curves (——) refer to DNS droplets. Upper dashed curves (- - -) refer to LES droplets with diffusion. Lower dashed curves (- - -) refer to LES droplets without diffusion.

[4] Berrouk, A. S., Laurence, D., Riley, J. J., Stock, D. E., 2007. Stochastic modelling of inertial particle dispersion by subgrid motion for les of high reynolds number pipe flow. Journal of Turbulence 8, N50.
URL `https://doi.org/10.1080/14685240701615952`

[5] Bragg, A., Collins, L., May 2014. New insights from comparing statistical theories for inertial particles in turbulence: I. Spatial distribution of particles. New Journal of Physics 16.

[6] Bragg, A., Collins, L., May 2014. New insights from comparing statistical theories for inertial particles in turbulence: II. Relative velocities. New Journal of Physics 16.

[7] Carrier, G., 1958. Shock waves in a dusty gas. Journal of Fluid Mechanics 4 (4), 376–382.

[8] Cernick, M., Tullis, S., Lightstone, M., 2015. Particle subgrid scale modelling in large-eddy simulations of particle-laden turbulence. Journal of Turbulence 16 (2), 101–135.
URL `https://doi.org/10.1080/14685248.2014.969888`

[9] Chan, C., Zhang, H., Lau, K., 2000. An improved stochastic separated flow model for turbulent two-phase flow. Comp. Mech. 24, 491–502.

[10] Chen, C., Wood, P., 1985. A turbulence closure model for dilute gas-particle flows. The Canadian Journal of Chemical Engineering 63 (3), 349–360.

[11] Chen, C., Wood, P., 1985. A turbulence closure model for dilute gas-particle flows. The Canadian Journal of Chemical Engineering 63 (3), 349–360.

[12] Chen, C., Wood, P., 2000. Turbulence closure of the dilute gas-particle axisymmetric jet. AIChE Journal 32 (1), 163.

[13] Chen, L., Goto, S., Vassilicos, J., 2006. Turbulent clustering of stagnation points and inertial particles. J. Fluid Mech. 553, 143–154.

[14] Chun, J., Koch, D., Rani, S., Ahluwalia, A., Collins, L., 08 2005. Clustering of aerosol particles in isotropic turbulence. Journal of Fluid Mechanics 536, 219–251.

[15] Clark, R., Ferziger, J., Reynolds, W., 1979. Evaluation of subgrid-scale turbulence models using a fully simulated turbulent flow. J. Fluid Mech. 91, 1–16.

[16] Crowe, C., Sharma, M., Stock, D., 1977. The particle-source-in cell (psi-cell) model for gas-droplet flows. J. Fluids Eng. 99 (2), 325–332.

[17] Crowe, C., Sommerfeld, M., Tsuji, Y., 1998. Multiphase Flows with Droplets and Particles. CRC Press, Boca Raton.

[18] Danon, H., Wolfshtein, M., Hetsroni, G., 1977. Numerical calculations of two-phase turbulent round jet. Int. J. Multiphase Flow 3 (3), 223–234.

[19] Falkovich, G., Fouxon, A., Stepanov, M., 2002. Acceleration of rain initiation by cloud turbulence. Nature 419, 151–154.

[20] Fede, P., Simonin, O., 2006. Numerical study of the subgrid fluid turbulence effects on the statistics of heavy colliding particles. Physics of Fluids 18 (4), 045103.
URL `https://doi.org/10.1063/1.2189288`

[21] Fede, P., Simonin, O., Villedieu, P., Squires, K., 01 2006. Stochastic modeling of turbulent subgrid fluid velocity along inertia particle trajectories. In: Proceedings of the 2006 CTR Summer Program. pp. 247–258.

[22] Fessler, J., Kulick, J., Eaton, J., 1994. Preferential concentration of heavy particles in a turbulent channel flow. Physics of Fluids. 6 (11), 3742–3749.

[23] Fevrier, P., Simonin, O., Squires, K., 2005. Partitioning of particle velocities in gas solid turbulent flows into a continuous field and a spatially uncorrelated random distribution; theoretical formalism and numerical study. J. Fluid Mech. 533 (5), 1–46.

[24] Fubiani, G., de Esch, H., Simonin, A., Hemsworth, R., Jan 2008. Modeling of secondary emission processes in the negative ion based electrostatic accelerator of the international thermonuclear experimental reactor. Phys. Rev. ST Accel. Beams 11, 014202.
URL `https://link.aps.org/doi/10.1103/PhysRevSTAB.11.014202`

[25] Fuchs, N.A., ., 1964. The Mechanics of Aerosols. Macmillan, New York.

[26] Fuchs, N., 1965. The mechanics of aerosols. Quarterly Journal of the Royal Meteorological Society 91 (388), 249–249.

[27] Fung, J., Hunt, J., Perkins, R., 2003. Diffusivities and velocity spectra of small inertial particles in turbulent-like flows. Proceedings of the Royal Society of London A: Mathematical, Physical and Engineering Sciences 459 (2030), 445–493.

[28] Gicquel, L., Givi, P., Jaberi, F., Pope, S., 2002. Velocity filtered density function for large eddy simulation of turbulent flows. Physics of Fluids 14 (3), 1196–1213.
URL `https://doi.org/10.1063/1.1436496`

[29] Golubkina, I., Osiptsov, A., Sakharov, V., 2011. Supersonic low-concentration dusty-gas flow past a plane cylinder in the presence of an oblique shock wave interacting with the bow shock. Fluid Dynamics 1 (46), 51–63.

[30] Govindarajan, B., Leishman, J., Gumerov, N., 2013. Particle-clustering algorithms for the prediction of brownout dust clouds. AIAA Journal 51 (5), 1080–1094.

[31] Gustavsson, K., Mehlig, B., Oct 2011. Distribution of relative velocities in turbulent aerosols. Phys. Rev. E 84, 045304.

[32] Gustavsson, K., Mehlig, B., 2011. Ergodic and non-ergodic clustering of inertial particles. EPL (Europhysics Letters) 96 (6), 60012.
URL `http://stacks.iop.org/0295-5075/96/i=6/a=60012`

[33] Gustavsson, K., Mehlig, B., 2016. Statistical models for spatial patterns of heavy particles in turbulence. Advances in Physics 65 (1), 1–57.

[34] Gustavsson, K., Meneguz, E., Reeks, M., Mehlig, B., Nov. 2012. Inertial-particle dynamics in turbulent flows: caustics, concentration fluctuations and random uncorrelated motion. New Journal of Physics 14.

[35] Healy, D., Young, J., 2005. Full Lagrangian methods for calculating particle concentration fields in dilute gas-particle flows. Proceedings of the Royal Society of London A: Mathematical, Physical and Engineering Sciences 461 (2059), 2197–2225.

[36] Hinze, J. O., 1987. Turbulence. McGraw-Hill.

[37] Hussaini, M., Zang, T., 1987. Spectral methods in fluid dynamics. Annual Review of Fluid Mechanics 19, 339–367.

[38] Ijzermans, R., Meneguz, E., Reeks, M., 2010. Segregation of particles in incompressible random flows: singularities, intermittency and random uncorrelated motion. J. Fluid Mech. 653, 99–136.

[39] Ijzermans, R., Reeks, M., Meneguz, E., Picciotto, M., Soldati, A., Jul 2009. Measuring segregation of inertial particles in turbulence by a full Lagrangian approach. Phys. Rev. E 80, 015302.

[40] Kerr, R., 1985. Higher-order derivatives correlations and the alignment of small-scale structures in isotropic numerical turbulence. J. Fluid

Mech. 153, 31–58.

[41] Kwak, D., Ferziger, J., Reynolds, W., 1975. Three-dimensional time-dependent simulation of turbulent flow. Report TF-5, Thermosci. Div., Dept. Mech. Eng. Stanford University.

[42] Lebedeva, N., Osiptsov, A., 2009. Structure of inertial-admixture accumulation zones in a tornado-like flow. Fluid Dynamics 1 (44), 68–79.

[43] Lebedeva, N., Osiptsov, A., Sazhin, S., 2013. A combined fully Lagrangian approach to mesh-free modelling of transient two-phase flows. Atomization and Sprays 23 (1), 47–69.

[44] Lilly, D., 1967. The representation of small scale turbulence in numerical simulation experiments. Proc. of IBM Scientific Computing Symp. on Env. Sciences, 195.

[45] Marble, F., 1970. Dynamics of dusty gases. Ann. Rev. Fluid Mech. 2 (1), 397–446.

[46] Marchioli, C., Mar 2017. Large-eddy simulation of turbulent dispersed flows: a review of modelling approaches. Acta Mechanica 228 (3), 741–771.
URL `https://doi.org/10.1007/s00707-017-1803-x`

[47] Marchioli, C., Salvetti, M., Soldati, A., Dec 2008. Appraisal of energy recovering sub-grid scale models for large-eddy simulation of turbulent dispersed flows. Acta Mechanica 201 (1), 277–296.
URL `https://doi.org/10.1007/s00707-008-0066-y`

[48] Masi, E., Simonin, O., Bédat, B., 2011. The mesoscopic Eulerian approach for evaporating droplets interacting with turbulent flows. Flow, Turbulence and Combustion 86 (3–4), 563–583.

[49] Maxey, M. R., 1987. The gravitational settling of aerosol particles in homogeneous turbulence and random flow fields. Journal of Fluid Mechanics 174, 441–465.

[50] Mell, W., Nilsen, V., Kosaly, G., Riley, J., 1994. Investigation of closure models for nonpremixed turbulent reacting flows. Physics of Fluids 6 (3), 1331–1355.

[51] Meneguz, E., Reeks, M., 11 2011. Statistical properties of particle segregation in homogeneous isotropic turbulence. J. Fluid Mech. 686, 338–351.

[52] Minier, j.-p., 03 2015. On Lagrangian stochastic methods for turbulent polydisperse two-phase reactive flows. Vol. 50 (2015). pp. 1–62.

[53] Monchaux, R., Bourgoin, M., Cartellier, A., 2012. Analyzing preferential concentration and clustering of inertial particles in turbulence. International Journal of Multiphase Flow 40, 1 – 18.

[54] Nigmatulin, R., 1990. Dynamics Of Multiphase Media. No. v. 2 in Dynamics of Multiphase Media. Taylor & Francis.

[55] Orszag, S., Patterson, G., 1972. Numerical simulation of three-dimensional homogeneous isotropic turbulence. Physical Review Letters 28 (2).

[56] Osiptsov, A., 1984. Investigation of regions of unbounded growth of the particle concentration in disperse flows. Fluid Dynamics 19 (3), 378–385.

[57] Osiptsov, A., 2000. Lagrangian modelling of dust admixture in gas flows. Astrophysics and Space Science 274, 377–386.

[58] Pakhomov, M., Terekhov, V., 2013. Comparison of the Eulerian and Lagrangian approaches in studying the flow pattern and heat transfer in a separated axisymmetric trubulent gas-droplet flow. Journal of Applied Mechanics and Technical Physics 54, 596–607.

[59] Pan, L., Padoan, P., 10 2010. Relative velocity of inertial particles in turbulent flows. Journal of Fluid Mechanics 661, 73–107.

[60] Pandya, R., Mashayek, F., 9 2002. Two-fluid large-eddy simulation approach for particle-laden turbulent flows. International Journal of Heat and Mass Transfer 45 (24), 4753–4759.

[61] Papoutsakis, A., 2008. Assessment of LES sub-grid models for turbulent reactive flows. Ph.D. thesis, University of London, Imperial College of Science, Technology and Medicine.

[62] Papoutsakis, A., July 2018. Extension of the fully lagrangian approach for the integration of the droplet number density on caustic formations. In: Proceedings of the 15th IMSE Conference. 15th International Conference on Integral Methods in Science and Engineering. Abstract accepted. Editor: P. Harris. Brighton, UK.

[63] Papoutsakis, A., Rybdylova, O., Zaripov, T., Danaila, L., Osiptsov, A., Sazhin, S., September 2016. Modelling of the evolution of a droplet cloud in a turbulent flow. In: Proceedings of the 27th European Conference on Liquid Atomization and Spray Systems ILASS-Europe. Paper MF-07. Editors: G. de Sercey and S.S. Sazhin. Brighton, UK.

[64] Phythian, R., 6 1972. Some variational methods in the theory of turbulent diffusion. J. Fluid Mech. 53, 469–480.

[65] Picciotto, M., Marchioli, C., Reeks, M., Soldati, A., 2005. Statistics of velocity and preferential accumulation of micro-particles in boundary layer turbulence. Nuclear Eng. Design 235, 1239–1249.

[66] Pope, S., 2000. Turbulent Flows. Cambridge University Press.
URL `https://books.google.co.uk/books?id=HZsTw9SMx-0C`

[67] Ravichandran, S., Govindarajan, R., 2015. Caustics and clustering in the vicinity of a vortex. Phys. Fluids 3 (27), 033305.

[68] Reeks, M., 1977. On the dispersion of small particles suspended in an isotropic turbulent fluid. J. Fluid Mech. 83, 529–546.

[69] Reeks, M., July 2013. Particle drift in turbulent flows: the influence of local structure and inhomogeneity. In: Proceedings of the SIG42 Conference on Synthetic Turbulence Models. Wroclaw, Poland.

[70] Reeks, M., 2014. Transport, mixing and agglomeration of particles in turbulent flows. Journal of Physics: Conference Series 530.

[71] Reeks, M. W., 1992. On the continuum equations for dispersed particles in nonuniform flows. Physics of Fluids A: Fluid Dynamics 4 (6), 1290–1303.
URL `https://doi.org/10.1063/1.858247`

[72] Robinson, A., 1956. On the motion of small particles in a potential field of flow. Communications on Pure and Applied Mathematics 9 (1), 69–84.

[73] Rogallo, R., 1981. Numerical experiments in homogeneous turbulence. Tech. Rep. N81-31508/NASA-TM-81315, Space administration - NASA. (VA US).
URL `http://opac.inria.fr/record=b1050956`

[74] Rudinger, G., 1964. Some properties of shock relaxation in gas flows carrying small particles. The Physics of Fluids 7 (5), 658–663.

[75] Saffman, P., 1962. On the stability of laminar flow of a dusty gas. Journal of Fluid Mechanics 13 (1), 120–128.

[76] Sazhin, S., 2014. Droplets and Sprays. Springer, London.

[77] Sazhina, E., Sazhin, S., Heikal, M., Babushok, V., Johns, R., 2000. A detailed modelling of the spray ignition process in diesel engines. Combustion Science and Technology 160, 317–344.

[78] Shotorban, B., Mashayek, F., 2005. Modeling subgrid-scale effects on particles by approximate deconvolution. Physics of Fluids 17 (8), 081701.
URL `https://doi.org/10.1063/1.2001691`

[79] Shotorban, B., Zhang, K., Mashayek, F., 2007. Improvement of particle concentration prediction in large-eddy simulation by defiltering. International Journal of Heat and Mass Transfer 50 (19), 3728 – 3739.
URL `http://www.sciencedirect.com/science/article/pii/S0017931007001895`

[80] Shrimpton, J., Haeri, S., Scott, S., 2014. Statistical Treatment of Turbulent Polydisperse Particle Systems: A Non-Sectional PDF Approach. Springer, London.

[81] Simonin, O., Deutsch, E., Minier, J., Jun 1993. Eulerian prediction of the fluid/particle correlated motion in turbulent two-phase flows. Applied Scientific Research 51 (1), 275–283.
URL `https://doi.org/10.1007/BF01082549`

[82] Soldati, A., Marchioli, C., 2009. Physics and modelling of turbulent particle deposition and entrainment: Review of a systematic study. International Journal of Multiphase Flow 35 (9), 827 – 839, special Issue: Point-Particle Model for Disperse Turbulent Flows.

[83] Soo, S., 1967. Fluid dynamics of multiphase systems. Blaisdell Pub. Co.

[84] Squires, K., Eaton, J., 1991. Preferential concentration of particles by turbulence. Phys. Fluids A 3 (5), 1169–1178.

[85] Tchen, C., 1959. Diffusion of particles in turbulent flow. Advances in Geophysics 6, 165–174.
URL `http://www.sciencedirect.com/science/article/pii/S006526870860103X`

[86] Tsirkunov, Y., Volkov, A., Tarasova, N., July 2002. Full Lagrangian Approach to the calculation of dilute dispersed phase flows: Advantages and applications. In: ASME Fluids Engineering Division Summer Meeting. Montreal, Quebec, Canada.

[87] Volkov, K., Emelianov, V., 2008. Particle Laden Gas Flows. Fizmatlit Publishing House, Moscow (in Russian).

[88] Wang, B., Xiong, Y., Qi, L., 2006. Shock-induced near-wall two-phase flow structure over a micron-sized particles bed. Shock Waves 15 (5), 363–373.

[89] Wang, L., Maxey, M., 1993. Settling velocity and concentration distribution of heavy particles in homogeneous isotropic turbulence. Journal of Fluid Mechanics 256, 27–68.

[90] Wilkinson, M., Mehlig, B., Bezugly, V., 2006. Caustic activation of rain showers. Phys. Rev. Lett. 97 (4), 048501.

[91] Wood, A., Hwang, W., Eaton, J., 2005. Preferential concentration of particles in homogeneous and isotropic turbulence. International Journal of Multiphase Flow 31 (10-11), 1220 – 1230.

[92] Xia, H., Nicolas, F., Punzmann, H., Shats, M., 2013. Lagrangian scale of particle dispersion in turbulence. Nat. Commun. 4, 1–8.

[93] Zaichik, L., Alipchenkov, V., 2007. Refinement of the probability density function model for preferential concentration of aerosol particles in isotropic turbulence. Physics of Fluids 19 (11), 113308.

[94] Zaichik, L., Alipchenkov, V., 2009. Statistical models for predicting pair dispersion and particle clustering in isotropic turbulence and their applications. New Journal of Physics 11 (10), 103018.

[95] Zaichik, L., Alipchenkov, V., Sinaiskii, E., 2008. Particles in Turbulent Flows. Wiley VCH, London.

[96] Zaichik, L., Pershukov, V. A., Sep 1996. Problems of modeling gas-particle turbulent flows with combustion and phase transitions. review. Fluid Dynamics 31 (5), 635–646.

[97] Zaichik, L. I., Simonin, O., 2006. Connection between two statistical approaches for modelling of particle velocity and concentrations distributions in turbulenct flow: The mesoscopic eulerian formalism and the two-point probability density function method. Physics of Fluids 18 (12), 5107.